Chemical Engineering Journal 529 (2026) 172935

Contents lists available at ScienceDirect

Chemical Engineering Journal

journal homepage: www.elsevier.com/locate/cej

On a tunable capacitive multi-osmosis (CMO) system: Hybrid-scale modeling and mechanistic insights

Shivang Rampriyan [a], Bahni Ray [a], Bijoy Bera [b,*]

[a] Department of Mechanical Engineering, Indian Institute of Technology Delhi, New Delhi, India
[b] Interfacial Physics Lab, Chemical Engineering Department, Delft University of Technology, Delft, the Netherlands

ARTICLE INFO

Keywords:
Capacitive multi-osmosis (CMO)
Computational fluid dynamics (CFD)
Forward osmosis (FO)
Desalination
Multiscale modeling
Numerical analysis
Electrical double layer

ABSTRACT

We propose a capacitive multi-osmosis (CMO) system that can operate both in Forward Osmosis (FO) and Reverse Osmosis (RO) modes, depending on the electric potential difference across the membrane. We employ a hybrid-scale modeling approach that integrates pore-scale and membrane-scale models to evaluate system performance. The two models have been unified and validated via numerical investigations and physical experiments on a generic FO system. Based on insights from our models, we identify three competing drivers of osmosis under an electric field—pressure gradient, electroosmosis, and an anomalous drag. In conventional electric-assisted FO systems, the electrodes participate in superfluous electrochemical reactions due to contact with the feed and draw solutions. In the CMO system, the electrodes are placed outside the system and exert their electric field without physical interaction with the solutions or any system components, thereby preventing any reactions. The non-contact electric fields generated when the system is subjected to controlled electric potential differences can significantly enhance the permeate recovery in an FO system, paving the way for FO scale-up.

1. Introduction

Global water resources face a pressing paradox. While the Earth contains copious reserves of water, a minuscule fraction of that is viable for human consumption. The world producing nearly 360 billion cubic meters of wastewater annually [1] further compounds a problem which was already aggravated by the uneven spatial distribution of usable water resources. Thus, contemporary circumstances warrant the development and deployment of efficient wastewater management technologies. Zero/minimal liquid discharge is one such approach [2]. It seeks to minimize wastewater volume, preferably to zero if practical, by recovering all usable water from the wastewater and leaving behind "waste." Pressure/Osmotically-driven membrane separation processes (P/OMSPs) are popular options for this recovery process [3,4]. Reverse Osmosis (RO) is the most adopted PMSP in existence, but it suffers from drawbacks like persistent fouling, high pressure requirements, and poor efficiency in handling concentrated feeds [5]. Forward Osmosis (FO), an OMSP that is essentially normal osmosis, addresses most of these challenges. While FO presents distinct advantages, it is accompanied by inherent limitations.

One drawback of FO is that it has not been scaled-up extensively and fails to supplant RO in commercial applications due to several reasons, for example, the requirement of an additional separation step to recover freshwater [6,7]. Another reason is the low permeate flux produced by FO [8]. Several authors have reported enhancements in the FO process through various means, ranging from membrane development to process design improvements [9–16]. To investigate the effects of influencing parameters on a process like FO, a trend of modeling the FO process via computational fluid dynamics (CFD) has emerged [5,10,17–19]. Typical membranes used in FO have an asymmetric structure with a selective layer for rejecting certain solutes, and a support layer for mechanical support [20]. Most CFD studies on FO typically ignore the concentration gradients within the selective layer and substitute it with a concentration jump boundary, primarily due to grid resolution dissonance and a lack of understanding of the internal structure of the ultrathin selective layer [10,18,21]. Given that the solute concentrations on both sides of the selective layer are different, it is incorrect to disregard the concentration gradient within the pores of the selective layer.

One method to improve FO performance and facilitate scale-up is the application of electrical assistance. Prior works have reported the enhancement of water flux through an electric field in both FO and RO

* Corresponding author.
E-mail address: b.bera-1@tudelft.nl (B. Bera).

https://doi.org/10.1016/j.cej.2026.172935
Received 18 August 2025; Received in revised form 22 December 2025; Accepted 11 January 2026
Available online 17 January 2026

systems [16,22–24]. Most of these studies are experimental. Numerically, electric-assisted FO has only been evaluated through nonequilibrium molecular simulations. Most of the corresponding configurations involve the use of electrodes in contact with the feed and draw solutions, leading to undesirable electrochemical reactions at the electrodes that hinder FO enhancement. Our system overcomes this drawback by conceptualizing a design that prevents physical contact between the electrodes and the solutions. It involves placing the entire module within electrodes of opposite polarity, and the system may be described as a capacitor 'filled' with the FO module as if it were a dielectric. The resultant electric field exists everywhere between the electrodes. Since the electric field is generated without the electrodes coming into contact with the feed and draw solutions, it is referred to as a "non-contact electric field."

To explore the effects of non-contact electric fields on FO systems (the electrodes are not in contact with the solutions and do not participate in electrochemical reactions), we must model the physics inside the pores of the selective layer, viz., fluid flow, electrostatics, and species transport. The assumption of cylindrical pores while modeling transport phenomena through ion-selective membranes has been rigorously validated in a range of investigations [25–31]. Recent studies on the mechanisms of solvent transport in polyamide TFC membranes suggest that pore flow models might better describe mass transfer through the thin selective layer than the solution-diffusion (SD) models [32–34]. These inferences, in part, stem from advancements in imaging technology. Special imaging techniques like positron annihilation spectroscopy [35] and modifications of transmission electron microscopy [36,37] confirm the existence of sub-nanometer pores within the thin polyamide selective layer, which was traditionally thought to be a dense layer subject to SD transport models [33,37].

Although the support layer morphology has been extensively characterized through scanning electron microscopy (SEM) [14,38,39], limited progress has been made in understanding the structure of the selective layer. Keeping this in mind, we would like to emphasize that the SD model has served as the gold standard for modeling membrane transport phenomena since decades and continues to provide reliable predictions across a wide range of osmotically driven processes. For example, a recent study [40] critically examines the claims against the SD model and demonstrates that many such observations can be reconciled within an appropriately formulated SD framework. For the present case with an applied non-contact electric field, our concern is not with the validity of the SD model, but that its classical formulation may not explicitly capture the new physics arising from the electric field–charge interactions within the selective layer. Our present work is an effort to develop and validate a hybrid modeling framework based on the principles of multiscale modeling [41–43] that complements the traditional CFD-based FO modeling approach by incorporating pore-scale electrokinetic effects in the selective layer, thereby enabling a more comprehensive evaluation of FO systems subjected to external, non-contact electric fields.

We consider our membranes to be charged when in contact with aqueous electrolytes. Due to the contact of the pore wall with the electrolyte, an Electrical Double Layer (EDL) develops within the fluid phase close to the pore wall. The EDL can be considered to be composed of two layers in tandem, one with predominantly immobile solvated counterions in contact with the wall surface (Stern layer), and the other containing a relatively large number of solvated counterions not bound to the wall surface and capable of movement along the pore axis (diffuse layer) [44]. The EDL is crucial to osmotically driven membrane separation processes (OMSPs) and membrane transport in general because it interacts with ions in the electrolytes and influences ion selectivity and water flux. In fact, fine-tuning the EDL characteristics can help develop programmable ion migration pathways [45]. The EDL is especially important for osmosis under an electric field, where solvent transport is governed by the motion of ions [46].

While not developed explicitly for FO systems, prior works have comprehensively investigated the aforementioned physics in charged micro/nanochannels. Burgreen & Nakache [28] provided one of the first analytical solutions to electrokinetic flows in very fine capillary channels with rectangular cross-sections, unlike their contemporary studies which considered channels with sufficiently large electrokinetic radii. Rice & Whitehead [47] extended their treatment to cylindrical capillaries, which closely represent the pores of modern FO membranes. Anderson & Malone [25] developed a 2D thermodynamic transport model for cylindrical membrane pores but failed to provide solutions for very small pores characteristic to FO membranes. Wyman & Kostin [48] proposed a numerical paradigm that coupled the Navier-Stokes (NS) equations for momentum transport with the Poisson-Nernst-Planck (PNP) equations to explain osmotic flow through membranes, although they emphasize 'anomalous osmosis.' Osmosis is typically understood as the movement of solvent from low to high concentrations of solute. However, anomalous effects have been observed during osmosis through charged membranes involving electrolytes, as determined by Grim & Sollner [49] in their intriguing experimental studies. Sasidhar & Ruckenstein [26] also adopt the PNP-NS formulation with the Boltzmann approximation and reinforce the results on anomalous osmosis in [49,50].

It is important to note that the connotations of the word "anomalous," as used in the above studies are vastly different from our understanding and construction of "anomalous" in "anomalous drag." Anomalous osmosis refers to osmosis observations contrary to conventional understanding of the process, while anomalous drag describes an anomalous driver of osmosis (further details in section 3.2). Nevertheless, Wyman & Kostin [48] were one of the first advocates for a full-scale Electrical Double Layer (EDL) resolution through the PNP-NS system without assuming the Boltzmann distribution for the ion concentration within the pore.

Patankar & Hu [51] developed a numerical formulation for simulating electroosmotic flows in complex geometries relevant to capillary electrophoresis devices. However, in their treatment, advective transport dominates diffusion and they do not explicitly solve the advection-diffusion equations for obtaining the concentrations of constituent species within the capillary channel, which is a necessity for FO models. Arulanandam & Li [52] present a detailed consideration of electroosmotic flow in rectangular microchannels and investigate the dependence of osmotic flow on the channel hydraulic diameter, aspect ratio, electrolyte concentration, and electric field strength. Their model does not explain electroosmosis through nanochannels because they use the Boltzmann distribution for determining the ionic concentration within their channels, which does not hold for nanochannels where the EDLs typically overlap [53].

Several of the aforementioned studies have served as the foundation for developing pore transport models for charged membranes under various operating configurations. Some of the corresponding approaches are outlined in [29,30,54]. Mehta & Morse [55] even proposed a membrane-scale cell model for explaining transport through charged membranes. Their model considers the membrane as an array of charged spheres, providing physical insights into the entire membrane, not just a pore. They describe pertinent results by applying their model to electrodialysis and hyperfiltration.

There is a general consensus in the literature that the key driver of osmosis is the hydrodynamic pressure gradient within the membrane, rather than the solvent concentration gradient [33,34,54,56,57]. While most of the foregoing studies have examined RO, which is a pressure-driven process, their insights are equally applicable to FO, an osmotically driven process. This is because FO and RO differ in their operation, but their underlying transport mechanisms are identical. In RO, an external hydraulic pressure generates an internal pressure gradient that overcomes the one that would otherwise arise naturally and drives solvent flow opposite to the 'normal osmosis' direction. In contrast, the pressure gradient in FO is not externally imposed but develops spontaneously from the difference in solvent chemical potential between the

feed and draw sides, which is thermodynamically equivalent to the osmotic pressure difference. Thus, the two processes differ in operation but share the same physical basis—solvent flow induced by a pressure gradient that acts to equalize the chemical potential field across the membrane.

However, in this study, we argue that while solvent concentration gradients are not required to explain osmosis, the pressure gradient may not necessarily be the primary driver responsible for osmotic flow. Instead, we propose that osmotic flow is better determined by a competing interaction between hydrodynamic, electroosmotic, electrophoretic, and diffusive forces, which encompass all possible physical effects enunciated by the governing equations for osmosis through charged membranes (see section 3.2). The dominating effects of the latter three forces over the pressure gradient were observed only when we performed detailed investigations on transport through the pores of a charged membrane subjected to an external electric field, which could be one of the reasons why the said forces have remained largely obscure in the relevant literature.

Based on the preceding discussions, it is worthwhile to investigate the effects of an external electric field on FO systems through a physical model, ensure a well-informed design, and explore scale-up opportunities. Thus, in this work, we present a comprehensive CFD-based hybrid model for an FO system enhanced by a non-contact electric field. We start with the membrane-scale model for the system and obtain the concentration polarizations (CP) in the process. We adjust the bulk solute concentrations in the feed and draw solutions for CP effects to find the ion concentrations on either side of the selective layer. We then transition to solve for the velocity, electric, and concentration fields using the PNP-NS system of equations and obtain the effects of potential difference across the selective layer, wall charge distribution, and the selective layer thickness on the flow and concentration fields in the system. More importantly, we explore the changes in the permeate flux due to variations in the different influencing parameters. From our simulations, we deduce some critical insights into the physical mechanisms that concertedly operate to effect osmosis through charged membranes subject to external electric fields. A wider application of our work promises an electrically-tunable CMO system that can work both in FO and RO modes.

2. Methodology

2.1. Implementation overview

The hybrid modeling approach proposed in this study follows a two-step iterative paradigm. In the first step, we employ the membrane-scale CFD model developed in our previous work to determine the solute concentration distribution within the baseline FO module (without an externally applied electric field) [17]. The solute concentrations on both sides of the selective layer are then extracted and used as inlet and outlet boundary conditions for the subsequent pore-scale model, which models a single representative pore. The water flux curve generated from the pore-scale simulations across multiple membrane pores is provided as a boundary condition to upscale the selective layer permeability used in the membrane-scale model. This process is repeated iteratively until the water flux distribution predicted by the pore-scale model converges with that obtained from the membrane-scale model. After the pore-scale model is validated through this coupling, all further analyses are performed using the pore-scale model alone. This was a deliberate choice motivated by physics, not simplification, because only the pore-scale model could fully capture the electrokinetic phenomena happening inside the selective layer after the system was subjected to an external electric field. We present a thorough description of this methodology in the following subsections.

2.1.1. Bridging the membrane-scale and pore-scale models

We first implemented a validated membrane-scale 2D CFD model to obtain the water flux (J_w) and the extent of CPs within the baseline FO system (without any electrical enhancements) for a desired combination of system parameters like feed and draw inlet concentrations ($c_{f,in}$ and $c_{d,in}$) and speeds ($u_{f,in}$ and $u_{d,in}$), membrane properties like porosity, tortuosity, water permeability, etc. The details of the model have been extensively described in our previous work [17]. Fig. 1(a) illustrates the overall geometry of the FO system with exaggerated sizes for the constituent membrane layers. Once the appropriate physical quantities are evaluated for different positions along the membrane, we can obtain the solute concentration on either side of the selective layer, that is, the feed solution-selective layer interface, and the selective layer-support layer interface (assuming that we operate our system with the selective layer facing the feed solution). Assuming a straight, cylindrical pore through the selective layer, we now know the solute concentrations on both its inlet and outlet at any arbitrary location on the membrane. Subsequently, the given concentrations are implemented in a pore-scale model described later. Through the pore-scale model, J_w^{pore} is obtained as the average volume flow rate per unit area through the outlet of the pore. If this pore-scale J_w is different from the membrane-scale J_w^{mem} by a magnitude exceeding a specified tolerance, the pore-scale J_w^{pore} is used to calculate an upscaled selective layer permeablity to be imposed as a boundary parameter in the membrane-scale model to recalculate the CPs and J_w^{mem}. Mathematically, the algorithm is stopped when the following condition is satisfied for all pore positions,

$$\frac{\left|J_w^{pore} - J_w^{mem}\right|}{\left|J_w^{pore}\right|} \leq TOL \tag{1}$$

where J_w^{pore} is the pore-scale local water flux ($\frac{\mu m}{s}$), J_w^{mem} is the membrane-scale local water flux ($\frac{\mu m}{s}$), and TOL is the set tolerance at 10^{-6}.

As illustrated in Fig. 1(b), we select 74 equidistant pores along the length of the membrane and repeat the validation process for each of them. However, the validation comparison data has been presented only for five distinct equidistant pores along the length of the membrane.

2.1.2. Experimental method

Besides numerical validation, we performed experiments on the baseline FO module by fabricating a lab-scale module made from laser-cut polymethyl methacrylate (PMMA) sheets. A thin-film composite (TFC) FO membrane (Sterlitech Inc., Auburn, USA) was sandwiched between feed and draw channels, each of identical dimensions (300 mm $\times$ 100 mm $\times$ 5 mm). The module was operated in FO mode, that is, the selective layer of the membrane faced the feed solution. No feed or draw spacers were used in the flow channels (see section 3.1 for a discussion on this decision). Two magnetic drive pumps (Promivac Pumps Pvt. Ltd., Noida, India) with a maximum rated flow of 900 LPH were used to circulate the feed and draw solutions through the module. Two electronic weighing scales (EXCELL weighing Pvt. Ltd., New Delhi, India), each with a capacity of 30 kg were used to perform mass measurements required to calculate the water flux. The experiments were conducted using aqueous NaCl solutions at varying concentrations. The crystalline, pure form of NaCl (Thermofisher Scientific India Pvt. Ltd., Mumbai, India) was dissolved in lab-grade deionized water to create the solutions. All measurements were performed in batch mode after the system was allowed sufficient time to attain a steady state. Further details on the experimental setup, measurements, and analyses can be found in supplementary section S1.

2.1.3. Parametric investigations

We now focus on the validated pore-scale model. The model invokes fundamental steady-state equations for fluid flow and species diffusion with appropriate modifications to incorporate electromigration effects. We then explore the effects of a diverse set of parameters like external voltage, solute valency, wall charge distribution, and pore length on the pore J_w, while offering critical insights on the mechanisms of forward

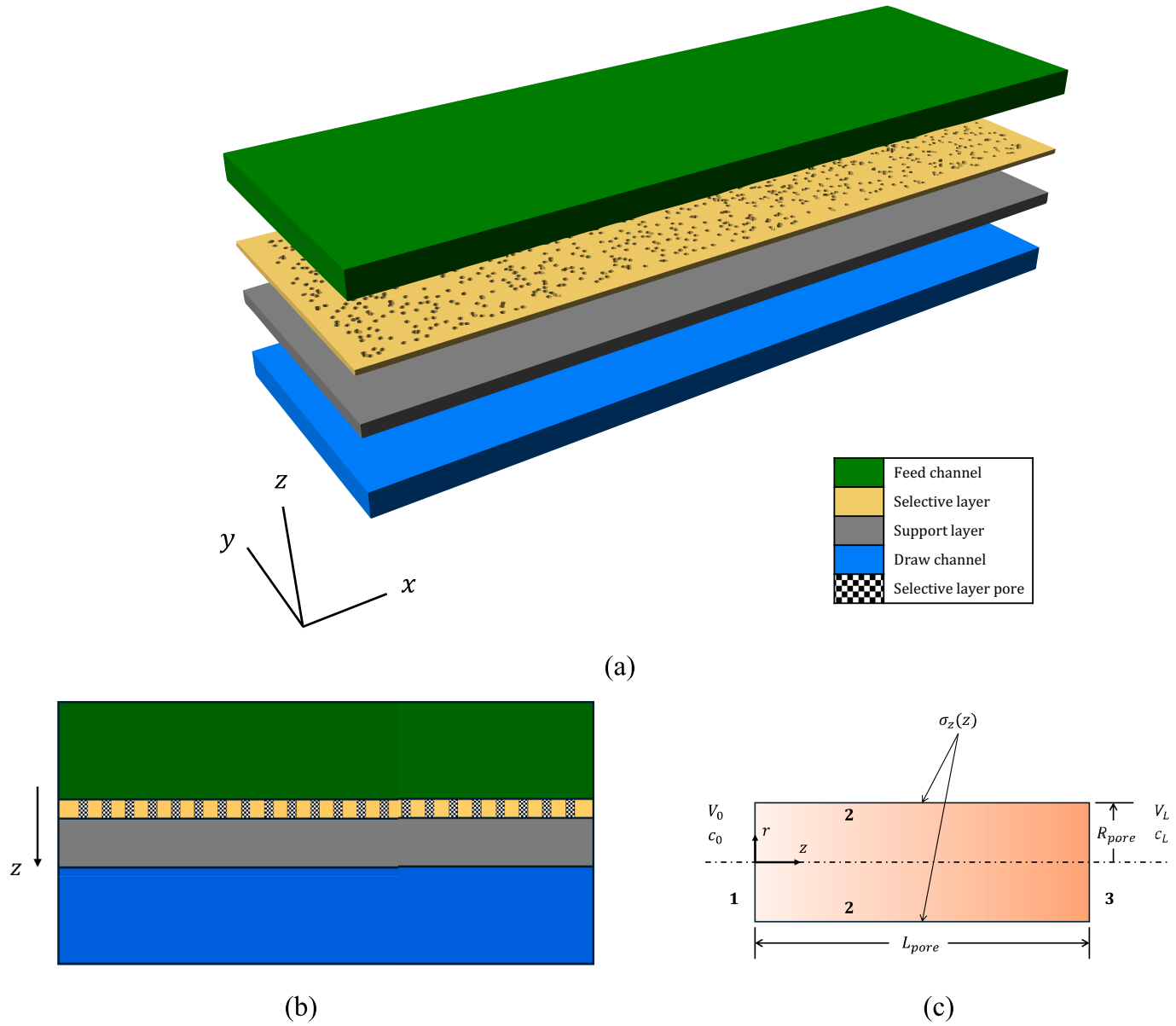

Fig. 1. Simulation domains for models constituting the hybrid-scale model. (a) 3D layout of the FO system. (b) Membrane-scale geometry representing the division of the selective layer into 74 pores (only 22 are shown, and results are reported for five equidistant pores as described in section 2.3.5), for further details on the simulations, see [17]. (c) Pore-scale geometry.

osmosis under the application of an external electric field.

2.2. Description of the model geometry

The model geometry is shown in Figs. 1(b) and (c). Fig. 1(b) illustrates the membrane-scale model geometry, and Fig. 1(c) depicts the pore-scale model geometry. In Fig. 1(c), the axis of the pore coincides with $r = 0$. The pore geometry is divided into three surfaces 1–3. Surfaces 1 and 3 indicate the inlet and outlet of the pore, respectively. Surface 2 is the inner curved surface of the pore, which contains a certain charge distribution (σ_z). The radius and length of the pore are R_{pore} and L_{pore}, respectively. All physical quantities (c, V) at 1 are marked with a subscript 0, while those at 3 are marked with the subscript L, corresponding to the z-positions of the surfaces. The solute concentration at 1 is less than the solute concentration at 3, so the natural osmotic flow is expected to be in the positive-z direction, driven by the chemical potential gradient (assuming all other conditions are identical at 1 and 3). There is an existing concentration gradient within the pore at steady state. The baseline case assumes a zero pressure difference between the inlet and the outlet.

2.3. Problem formulation

In the following subsections, estimate the pore wall surface charge, pore dimensions, and the electric potential difference across the pore.

2.3.1. Surface charge

Most surfaces gain a surface electric charge when brought into contact with a polar phase. The electric charges at the interface tend to redistribute themselves in a certain manner [44,52]. The discussion can be extended to the present study considering the membrane is in contact with the feed and draw solutions. Surface 2 is the pore wall in contact with electrolyte solution and is laced with a surface charge with some distribution $\sigma_z(z^*)$ along the length of the pore, where $z^* = \frac{z}{L_{pore}}$. Since we assume a cylindrical pore, we leverage its symmetry about the central axis to reduce our analysis domain to half of the pore. The final model

geometry is given in Fig. 2. If $c_0 < c_L$, one would expect a solvent flow from surface 1 to surface 3. As we noted in section 2.2, we assign a surface charge to the pore wall. However, the calculation of surface charge and its distribution along the pore wall is not straightforward as described in the following paragraphs.

First, we use the Grahame equation quoted in [58] to obtain surface charge from zeta potential (ζ_0) data, which is relatively more abundant in literature than direct surface charge data. Zeta potentials, and consequently, the surface charge values, for polyamide TFC membranes were extracted from [13,59,60]. Using the zeta potential to obtain wall surface charge exposes our model to an intrinsic limitation. The zeta potential is the electric potential at the shear plane of the EDL [52,61], and since we use the zeta potential to characterize the surface charge of the pore wall, the pore wall we use in our model is not the 'real' pore wall, but an 'imaginary' pore wall that coincides with the shear plane. This approximation is reasonable because within the shear plane, the ions are considered immobile due to ion-specific effects like surface dissolution or adsorption [44,52]. In a previous section, we mentioned how the EDL comprises the immobile Stern layer and the mobile diffuse layer. Although the Stern layer is a part of the EDL, its potential drop is implicitly included in the zeta potential. Therefore, the coupling between the Stern and the diffuse layers is indirectly accounted for through the zeta potential-based boundary condition. Since our focus is on ion transport and electrostatic effects beyond the shear plane, this treatment provides an accurate and widely accepted representation of the electrostatic boundary condition. Henceforth, all references to "pore wall" in our study will imply the shear plane of the EDL under consideration.

The value for the wall surface charge for the pore wall was $-0.0180\,\frac{C}{m^2}$ when the solute was NaCl, and $0.0243\,\frac{C}{m^2}$ when the solute was $MgSO_4$. These values were not varied unless specified in the study. While the average value of the surface charge was kept constant, there is no reason for the charge to be uniformly distributed on the pore wall, as indicated through investigations performed in [62,63]. For all baseline cases, we distributed the surface charge between 20% and 80% of the pore length and variations in the charge distribution were considered via parametric studies.

2.3.2. Pore dimensions

Advanced techniques mentioned earlier have rekindled the interest in understanding the selective layer morphology and geometry. We assign the values $R_{pore} = 8$ Å for the pore radius, and $L_{pore} = 2000$ Å for the pore length, following the values reported in literature [33,37,64]. Here, L_{pore} is identical to the selective layer thickness.

2.3.3. Electric potential difference across the pore

Referring to Fig. 1(a), we observe three components constituting the plate-and-frame FO module—the feed and draw channels, and the membrane with its selective and support layers. Assuming the two plates enclosing the flow channels to be made of PMMA, each with an outer thin sheet of stainless steel, we introduce a potential difference between the feed and the draw sheets. The stainless-steel sheets act as electrodes for the CMO setup (see supplementary section S2). Our arrangement is unlike prior studies on electrically enhanced osmotic processes, where the electrodes were placed within electrolyte and interacted with the ions in the system through oxidation and reduction mechanisms [16,24,65]. In our case, the electrodes are assumed to be non-interacting because they are separated from the electrolytes through PMMA slabs.

For our investigations, only the electric potential difference across the selective layer of the membrane (ΔV) is important. From ΔV, the potential difference across the entire module, ΔV_{mod}, may be obtained using a parallel plate capacitance model. The liquid domains of the feed and draw channels, the PMMA slabs, as well as the membrane, can be approximated as dielectric slabs. We include the effects of flow and solute concentration on the dielectric constant of the electrolytes following the works of [66,67]. The calculations regarding the necessary ΔV_{mod} to produce a desired ΔV are worked out in supplementary section S2. Table 2 in section 2.3.4 provides the ΔV_{mod} values corresponding to the ΔV used in the present work. A quick look at the table indicates that all ΔV_{mod} values are reasonable. However, ΔV_{mod} is several orders of magnitude higher than ΔV due to the ultrathin selective layer.

2.3.4. Governing equations and boundary conditions

At steady state, fluid flow inside the pore can be described through the mass continuity and Navier-Stokes equations where the effects of the external electric field are incorporated in the latter as a body force term. At steady state, the weakly compressible form of the continuity equation is given as,

$$\nabla \bullet (\rho \boldsymbol{u}) = 0 \tag{2}$$

where ρ is the fluid mass density, which is the arithmetic mean of the density contributions from the anions and cations (further details may be found in section 2.3.3), $\boldsymbol{u}$ is the fluid velocity with $\boldsymbol{u} = u_r \boldsymbol{e_r} + u_z \boldsymbol{e_z}$. The azimuthal component of the velocity is dropped due to the assumed axisymmetric nature of the pore. The weakly compressible form of the Navier-Stokes equations is written as,

$$\rho(\boldsymbol{u} \bullet \nabla)\boldsymbol{u} = \nabla \bullet \left[-p\boldsymbol{I} + \mu\left(\nabla \boldsymbol{u} + (\nabla \boldsymbol{u})^T\right) - \frac{2}{3}\mu(\nabla \bullet \boldsymbol{u})\boldsymbol{I} \right] + \boldsymbol{f_e} \tag{3}$$

where p is the hydrodynamic pressure, μ is the dynamic viscosity of the fluid, which is the arithmetic mean of the viscosity contributions from the anions and cations (further details may be found in section 2.3.3), $\boldsymbol{I}$ is the 3×3 identity matrix, and $\boldsymbol{f_e}$ denotes the electrical body force on the fluid due to ions within the solution being subjected to the external electric field. If we assume no slipping between the ions and the fluid, the fluid is dragged by the ions with a force equal to that exerted on the ions themselves. This approach has been extensively used in prior studies [51,52]. Thus, $\boldsymbol{f_e}$ can be written as,

$$\boldsymbol{f_e} = \rho_v \boldsymbol{E} \tag{4}$$

where ρ_v is the volumetric space charge density, and $\boldsymbol{E}$ is the electric field.

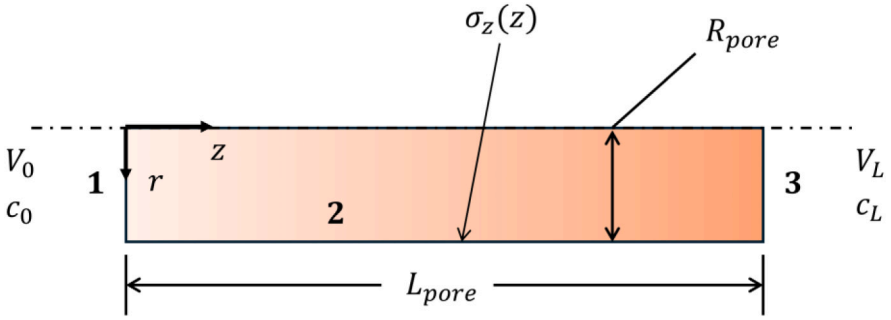

Fig. 2. Leveraging the axisymmetric nature of the pore-geometry in Fig. 1(c), it is possible to reduce the computational domain to half the original.

It is well-known that the divergence of the electric displacement vector is equal to the volumetric space charge density. Assuming the fluid flowing through the pore to be a linear, homogeneous, and isotropic dielectric medium with instantaneous response to changes in electric field, we can relate the electric field $\boldsymbol{E}$ with the space charge density ρ_v as,

$$\nabla \bullet \boldsymbol{E} = -\frac{\rho_v}{\epsilon} \tag{5}$$

where ϵ is the permittivity of the medium. Using the relationship between electric field $\boldsymbol{E}$ and electric potential Φ ($\boldsymbol{E} = -\nabla\Phi$), we can relate the electric potential and the space charge density as,

$$\nabla^2\Phi = -\frac{\rho_v}{\epsilon} \tag{6.1}$$

$$\text{with } \rho_v = F(z_a c_a + z_b c_b) \tag{6.2}$$

where F is the Faraday constant, z_a and z_b refer to the charges on the cations and anions respectively, and c_a and c_b imply the concentrations of the cations and anions, respectively. The azimuthal component of the equation is dropped due to the assumed axisymmetric nature of the pore. At this point, most studies tend to use the Boltzmann distribution equation to express c_a and c_b as a function of the bulk electrolyte concentration and the electric potential [28,47,52,55,68,69].

The Boltzmann equation assumes an inherent electroneutrality in the bulk fluid [28,52], which is an assumption valid only for a high value of electrokinetic parameter. For our modeling domain, we define the electrokinetic parameter β as the ratio of the pore radius to the characteristic EDL thickness (reciprocal of the Debye-Hückel parameter, see [61]). Thus,

$$\beta = R_{pore}\sqrt{\frac{2\omega^2 e^2 \bar{c} N_A}{\epsilon k_B T}} \tag{7}$$

where ω is the valency of the ions in the symmetric solute, e is the electronic charge, $\bar{c} = \frac{c_0+c_L}{2}$ is the average solute concentration in the pore, N_A is the Avogadro constant, k_B is the Boltzmann constant, T is the temperature (assumed constant at 298.15 K). Rice & Whitehead [47] in a prior study on the electroosmotic flow within a cylindrical capillary have reported a marked divergence from the plug-like electroosmotic velocity profile for $\beta < 10$. They attribute this observation to a double-layer overlap near the capillary axis. Substituting the corresponding baseline values with $\omega = 1$ and $\bar{c} = 0.31$ M (see section 2.3.4), we obtain $\beta = 1.4299$, which implies that the thickness of the EDL is comparable to the pore radius, and hence the assumption of electroneutrality in the bulk solution away from the pore wall is invalid. Another assumption within the Boltzmann equation is regarding axial gradients. It assumes that the variations in Φ, c_a, and c_b along the axial direction are insignificant compared to the radial variations [53]. However, given the externally imposed gradients on Φ, c_a, and c_b along the length of the pore, this assumption is incorrect.

To solve for c_a and c_b, we invoke the extended form of the steady state Nernst-Planck equations with an electromigration term and without any species generation due to chemical reactions [48,70] where the sum of divergence of the solute flux and the convection term is zero. The equations for the cations and anions can be written together as,

$$\boldsymbol{u} \bullet \nabla c_i = \nabla \bullet \left(D_i \nabla c_i + \frac{F}{RT} z_i D_i c_i \nabla \Phi \right) \tag{8}$$

where i can be a or b for the cations or anions respectively, D_i is the diffusion coefficient of the ion i in an aqueous solution, R is the universal gas constant, and $\frac{F}{RT} z_i D_i c_i \nabla\Phi$ is the electromigration.

From Eqs. (2)–(8), we can observe that there exists a five-way mathematical coupling between the weakly compressible fluid flow, species transport, and the electrostatic equations. These relationships are illustrated in Fig. 3(a). The five-way coupling between the three types of physics in the model makes the computations involved in obtaining the solutions to the modeling equations tedious. To reduce computation time and resource consumption, we suggest an order of magnitude analysis on Eq. (8) with the following scales for the relevant physical quantities— $r \sim R_{pore}$, $z \sim L_{pore}$, $u_z \sim J_w$, $u_r \sim \frac{R_{pore}}{L_{pore}} J_w$ (from Eq. (2)), $c_i \sim \frac{c_0+c_L}{2}$, $\Phi \sim \zeta_0$. In addition, we already know the values of the constants F, R, T, z_i, D_i. On the completion of this exercise (see supplementary section S3 for the detailed procedure), we find that the order of magnitude for the convective terms on the left-hand side of Eq. (8) is much less than for the diffusive and electromigration terms on the right-hand side. Therefore, the convective terms can be neglected from our analysis without compromising the quality of the results. The final coupling in the system of equations is four-way and much easier to compute than the previous five-way coupling, as shown in Fig. 3(b).

To close the system of equations of fluid flow, solute transport, and electrostatics, we need unique boundary conditions at every boundary of the domain. Surface 1 is the inlet of the pore where we set a constant gauge pressure p_0, ion concentration c_0, and electric potential V_0, each for the fluid flow, solute transport, and electrostatic equations, respectively. Similarly, at surface 3, we have the outlet of the pore where we assign a gauge pressure $p_L = p_0$, ion concentration c_L, and electric potential $V_L = 0$, unless specified otherwise. Since our domain is symmetric around the axis, the gradients of all physical quantities normal to the axis must vanish. Surface 2 being the curved surface, we assign a no-slip or separation boundary condition, no-solute flux boundary condition, and a finite surface charge density σ_z. They are illustrated diagrammatically through Fig. 4.

It is important to note that in the present work, the effects of the electric field have been confined to the selective layer and the corresponding influence at the system-scale has been quantified using the hybrid model (further details in section 2.3.8). This is a reasonable choice because the support layer has pores with diameters of the order of a few μm, and the corresponding β will be very high. Therefore, within the support layer, we expect the species transport to be dominated by the bulk advection due to the draw solution instead of electrokinetic phenomena due to the external electric field. Additionally, here may be skepticism about our use of continuum models to simulate phenomena occurring in a nanometer scale pore. However, we present a detailed argument on why our approach works for the present system in the supplementary section S7.

2.3.5. Material properties of the aqueous solutions

We produce our results for symmetric electrolytes—aqueous NaCl (monovalent) and aqueous $MgSO_4$ (divalent). The mass density and dynamic viscosity of the solutions were extracted from OLI Stream Analyzer (OLI Systems, Inc.), and the diffusion coefficients were obtained from the works of Rard & Miller [71,72]. We use a cubic spline interpolation method with continuous second derivatives to obtain the fluid properties at data points not covered through the software or experiments.

2.3.6. System parameters

Table 1 lists the relevant parameters and their values used in our study. Table 2 provides the values of ΔV_{mod} corresponding to the ΔV implemented in the simulations (see supplementary section S2).

2.3.7. Numerical paradigm and grid independence

The four-way coupling between Eqs. (2), (3), (6.1), (8), along with the boundary conditions specified in Fig. 4, yield a system of equations which can be solved numerically. We use a finite element software, COMSOL Multiphysics™, to solve the system of equations. The software has been extensively used to solve and simulate membrane processes under the influence of an electric field and without it in past studies

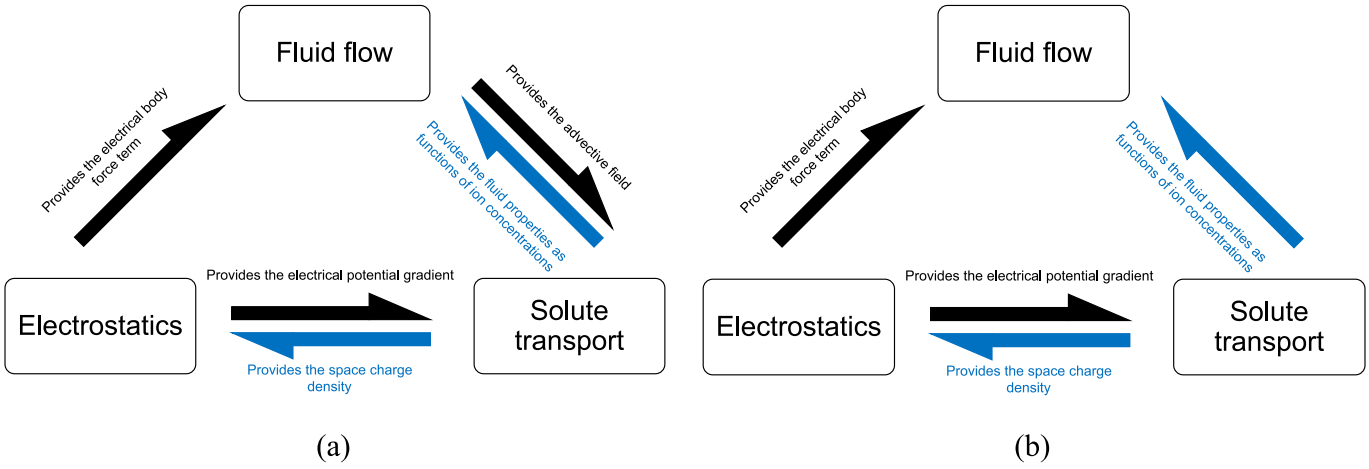

Fig. 3. Framework and interactions among the mathematical equations used to describe the model. (a) Five-way coupling of the relevant physics. (b) Reduced four-way coupling.

Table 1
System parameters used in the hybrid-scale model.

Category	Parameter name (unit)	Symbol	Value(s)
Module geometry	Module length (mm)	L	300
	Feed & draw channel thicknesses (mm)	$t_{c,f}$ & $t_{c,d}$	5
	Feed & draw inlet speeds (m/s)	$u_{f,in}$ & $u_{d,in}$	0.19
Operating configuration	Feed inlet solute concentration (M)	$c_{f,in}$	0.2
	Draw inlet solute concentration (M)	$c_{d,in}$	0.3, 0.4, **0.5**[x], 0.6, 0.7
Selective layer & its pores	Pure water permeability (m^2-s/kg)	A	3.18×10^{-12}
	Pore radius (Å)	R_{pore}	8
	Pore length (Å)	L_{pore}	500, 1000, 1500, **2000**, 2500
	Pore wall charge density (C/m^2)	$\sigma_z(z^*)$	−0.0180 for NaCl[#] 0.0243 for $MgSO_4$[#]
	Electric potential difference across the selective layer (ΔV)	mV	Context-specific
	Porosity	ε	0.70
Porous support layer	Tortuosity	τ	1.50
	Thickness (μm)	t_{PSL}	100
	Pure water permeability (m^2)	κ	2×10^{-15}

[x] : wherever multiple values of a certain parameter are available, the baseline value is indicated in boldface font.

[#] : while the charge density on the pore wall is constant, depending on the study objectives, the distribution of wall charge may vary. For example, a 40% charge spread with uniform wall density centered at $z^* = 0.5$ is the standard used in most test cases in the current work. However, we deal with different extents of charge spreads centered at different axial locations along the pore in several sections of our study. In addition, to impart a realistic representation to the wall charge distribution, σ_z, originally a step-function, was smoothed by introducing finite transition zones and continuous second derivatives at the step boundaries. The smoothed wall charge distributions are illustrated in the supplementary section S6.

[17,73–76]. Quadratic shape functions were used to interpolate between element nodes within the solution domain for obtaining the electric potential, velocity, pressure, and concentration fields. The physical couplings were rigorously implemented into the model by using the weakly compressible formulation of the Navier-Stokes equations along with the electromigration coupling between the electric potential and concentration fields.

Table 2
Values of ΔV_{mod} corresponding to ΔV values used in the present work (all other parameters at baseline values).

ΔV (mV)	ΔV_{mod} (V)
0	0
±2	±118.86
±4	±237.72
±6	±356.59
±8	±475.45
±10	±594.31

During the validation study, we split the membrane domain into 75 equidistant segments along its length and create 74 pores. Every segment has two extremities with one pore assumed to be stationed at each extremity, while ignoring the redundant pores. The membrane-scale model was run at the baseline configuration, and data regarding the water flux, solute concentration at the selective layer-feed solution interface, and solute concentration at the selective layer-porous support interface were obtained from the results using the COMSOL-MATLAB LiveLink™ feature. The obtained data was fed into the pore-scale model, and the model was solved for different inlet and outlet concentrations using the software's batch sweep functionality, providing the water flux value for each sweep instance. We fed the flux values obtained from the pore-scale model instances into the MATLAB™ script to obtain the relative error as outlined in Eq. 1, and relative errors for all pores were recorded in a 74×1 vector. We then compare the magnitudes of the errors stored within the vector against *TOL* and run the membrane-scale model with a water flux boundary condition that uses the flux obtained through the pore-scale model (see section 2.3.8 for the details). The process is repeated for the pores till the relative errors become less than *TOL*. The final flux results that were reported in this study were for equidistant pores placed along the membrane at 50 *mm*, 100 *mm*, 150 *mm*, 200 *mm*, and 250 *mm* from the feed inlet.

Since our geometry is a regular axisymmetric cylinder, we employ a structured mesh to discretize the simulation domain. The baseline model was discretized into 75,000 rectangular elements, with the sizes of the element dimensions ranging from 0.019 Å to 0.664 Å and a maximum growth rate of 1.13. 50 elements with an element ratio 3 were used to discretize the domain along the radial (r) direction, and 1500 elements with an element ratio 5 were used along the axial (z) direction. The element growth rates were exponential for both cases, and the size distribution was symmetric for the z direction, and monotonous for the radial direction. In the z direction, the mesh was increasingly finer toward the center to accurately capture the phenomena in the region with

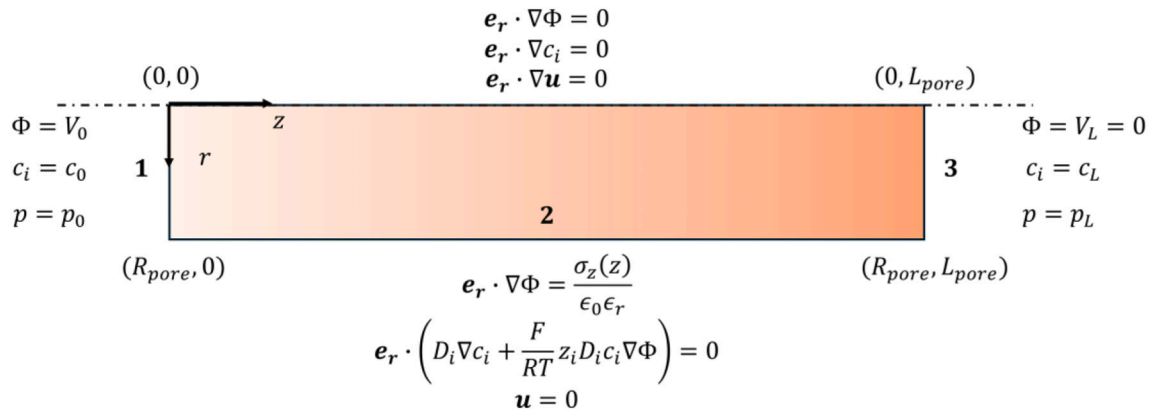

Fig. 4. Boundary conditions used for solving the system of equations generated by the collection of Eqs. (2)–(8). The constraints imposed on each boundary are listed near the corresponding boundary.

surface charge. In the radial direction, the mesh was monotonously sparser toward the axis because a finer mesh would help resolve the EDL effects in the regions near the surface charge, and such effects may be of greater interest than those occurring near the axis of the pore. A grid independence study was performed with *MN* varying from 20 to 70 in intervals of 5, where the mesh number, *MN*, is the number of domain divisions in the radial direction, and the total number of elements is given as $30MN^2$. Further details about the meshing and grid independence tests may be found in supplementary section S4.

The parallel direct sparse solver (PARDISO) was used to solve the system of equations. PARDISO implements a supernodal method, a form of Gaussian elimination for large sparse systems of equations [77,78]. We allow row and reuse preordering along with Bunch-Kaufman pivoting [79]. All the simulations were performed on a PC with a 16-core 12th generation Intel™ i5 processor, 4 GB NVIDIA GeForce RTX3050i graphics, 16 GB RAM. The study times ranged from a few minutes to a few hours, depending on the type of parameters studied. The simulation framework is presented pictorially in Fig. 5.

2.3.8. Hybrid model algorithm

The hybrid model couples the membrane-scale CFD model with the pore-scale selective layer model through an iterative exchange of fluxes and interfacial concentrations. The membrane-scale model [17] is first solved using baseline operating conditions (Table 1 and [17]) to obtain the water flux along the membrane $J_w^{mem}(x)$, where x is the coordinate along the membrane's length, and the solute concentrations at the feed (c_0) and support layer (c_L) interfaces of the selective layer. At this stage, the membrane-scale model does not include electric-field effects.

These interfacial concentrations are then imposed as boundary conditions for the pore-scale model, which explicitly accounts for electrokinetic effects within the selective layer. This is a necessity because the membrane-scale model does not account for the said effects. Solving the pore-scale model yields an electric-field-augmented local water flux $J_w^{pore}(x)$, where x is the coordinate of pore position along the membrane's length.

To transfer pore-scale electrokinetic effects back to the membrane-scale model, an upscaled selective layer permeability $A(x)$ is evolved according to $A_{i+1}(x) = A_i(x) \times \frac{J_{w,i}^{pore}(x)}{J_{w,i}^{mem}(x)}$, where i is the iteration index. For the first iteration, $A_1(x) = A$, which is a constant value listed in Table 1. Since $J_{w,i}^{pore}(x)$ is available only at the pores, $A_i(x) \forall i > 1$ will be available only for the pore positions. We interpolate the permeability values to obtain $A_i(x)$ for locations between the pores and thus all points along the membrane's length.

Once the upscaled permeability is obtained, the membrane-scale model is then re-solved to obtain revised values of $J_w^{mem}(x)$ and the corresponding interfacial concentrations, which are again supplied to the pore-scale model. This procedure is repeated until the pore-scale and membrane-scale fluxes converge within a prescribed tolerance as described in section 2.1.1. A representative convergence history for the

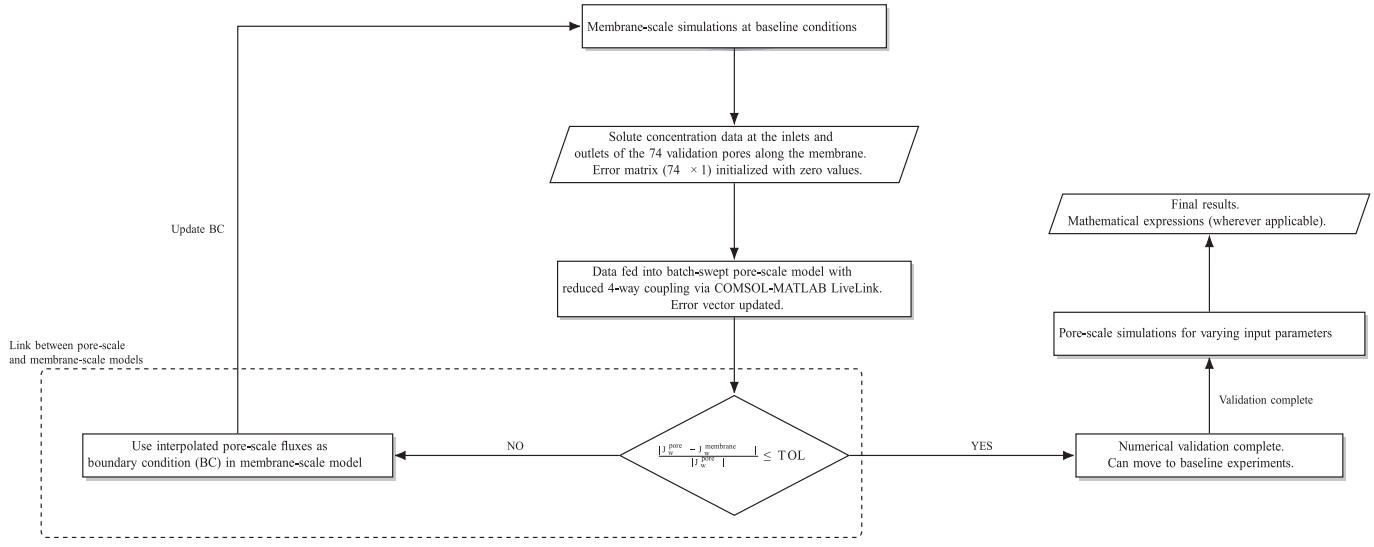

Fig. 5. Flowchart for the simulation framework—includes validation implementation.

baseline $\Delta V = 3\,mV$ is shown in Fig. 6(b).

3. Results and discussion

3.1. Numerical and experimental validation

There are extant experimental studies on an electrically assisted forward osmosis system where the electrodes interact with the feed/draw solutions through pH balancing mechanisms or ion transfer [16,24,65]. However, there is limited literature on electrically-assisted FO systems where the electrodes are not in contact with the electrolytes and do not interact with the FO module except by producing an electric field which then affects the flow and concentration fields within the module. Therefore, we do not have direct experimental data to validate our model for the electrically-enhanced cases and adopt indirect validation methods as elucidated in this section.

1. The first test case is run with the setting $\Delta c = c_0 - c_L = 0$ and the other parameters being identical to the baseline model. As expected, in the absence of pressure, electric potential, and concentration gradient, there is no overall flow in the pore. The case is also tested for $\sigma_z(z^*) \equiv 0$, and the results are similar.
2. The second test case is run with $\Delta c = c_0 - c_L = 0$, $\sigma_z(z^*) \equiv 0$, $\Delta V = 0$, and $\Delta p = p_0 - p_L = 1\ bar$. For this case, we obtained the classic Poiseuille flow profile. The profiles obtained are validated against the Hagen-Poiseuille equation as outlined in supplementary section S5. An excellent agreement is found between the results obtained from the model and the profile predicted by the equation.
3. Rice & Whitehead [47] report the trends in the axial velocity (u_z) along the radius of the capillary for multiple values of β. For $\beta \leq 2$, the profile becomes increasingly Poiseuille-like, which is also observed in our model with $\beta = 1.4299$.
4. In the fourth case, we have a non-zero $\sigma_z(z^*)$ within the pore, $\Delta c < 0$, and $\Delta p = 0$. The validation for this case is done using the CFD model implemented in [17]. The flux is expected to be driven from $z^* = 0$ to $z^* = 1$. The details of the hybrid model have been provided in section 2.1. We present the validation through a comparison between the water flux predicted by the membrane-scale model at five representative pores along the length of the membrane in the direction of the flow and that predicted by the pore-scale model. The validation is also supported by our experimental results, aligning with the modeling results. All insights are illustrated in Fig. 6(a). In section 2.1.1, we mentioned that no spacers were used in the module. Spacers are commonly employed in FO modules to enhance fluid mixing near the membrane surfaces, increase shear, and reduce concentration polarization, thereby improving water recovery [80]. They also provide mechanical support to the membrane, preventing deflection or collapse under hydrodynamic stresses. However, the objective of the present study is validation rather than performance enhancement. The presence of spacers may introduce flow non-uniformities and localized fouling near spacer filaments, even when the pressure drop in a plate-and-frame module is marginal. Their omission in the current setup helps maintain well-defined hydrodynamic conditions and isolate the intrinsic membrane transport behavior. Mechanical integrity is not a concern under the nominal operating pressures employed, and the simplified configuration allows a more direct comparison between experimental observations and model predictions. From Fig. 6(a), we observe that the pore-scale model agrees well with both the membrane-scale model and the experimental results. The highest error between the J_w values obtained from the respective models is 12.13% when the difference between $c_{f,in}$ and $c_{d,in}$ is 0.1 M at $z^* = \frac{1}{6}$. The model works well as the gap between $c_{f,in}$ and $c_{d,in}$ widens, and the errors remain around 5% with the minimum error being as low as 2.53% for $c_{d,in} = 0.6\,M$ and $z^* = \frac{5}{6}$. Since the draw solution collects water from the feed solution as it moves tangential to the membrane, it becomes increasingly diluted, lowering the effective osmotic pressure gradient across the membrane, and thus, J_w. The J_w curves demonstrate a decreasing nature, further confirming this trend.

We have used a continuum formulation to explain the physical phenomena occurring in the selective layer pore. Thus, there may be concerns about its applicability at the nanometer-scale, and one may argue that molecular dynamics simulations may be better suited to the present work. This argument is not incorrect. Nevertheless, the continuum formulation still gives satisfactory results due to the reasons outlined in Supplementary section S7.

To further confirm the applicability of the hybrid model, we test it for $\Delta V = 3\,mV$ and all other parameters at the baseline level. The results are shown in Fig. 6(b). We observe that eight iterations are required to achieve convergence between the pore-scale and membrane-scale water flux. For the case of $\Delta V = 0$, the pore-scale and membrane-scale models yield agreeable results in a single iteration, as illustrated in Fig. 6(a). At $\Delta V = 0$, the membrane-scale selective layer permeability (A listed in Table 1) already represents the selective-layer transport accurately. No additional iterations are required because no additional pore-scale physics is introduced; therefore, the membrane-scale and pore-scale models are already consistent for identical operating parameters. Small residual differences between pore-scale and membrane-scale fluxes arise from differences in spatial averaging and model resolution and are within acceptable scientific limits.

3.2. A note on the mechanism of osmosis assisted by an electric field

Through a detailed analysis of the cases considered in our study (presented in the following subsections), we observe that the net osmotic flow between symmetric electrolytes of different concentrations separated by a membrane subject to an external electric field is a cumulative effect of the following driving forces—1) hydrodynamic pressure gradient induced due to EDL formation, 2) electroosmotic flux due to body force generated by the net electric field, 3) diffusive ion flux, 4) electrophoretic ion flux. Of these, the hydrodynamic pressure gradient has been identified as the key driving force for osmosis in several prior works [56,57]. Electroosmosis as a physical phenomenon has also been comprehensively investigated [46,51,52,69]. However, attention to the role of diffusive and electrophoretic ion fluxes on explaining osmotic phenomena has been lacking. The line of thought in including the latter two fluxes in determining the net osmotic flow is as follows. Assuming zero slip between the ions and solvent molecules (in this study, water molecules), if electroosmotic effects can drive the solvent in a specific direction due to asymmetric forces on the ions within the EDL, so can the diffusive and electrophoretic effects on the ions within the EDL. It may very well be observed that the three fluxes compete against each other and the pressure gradient to determine the net flow, as will be further elucidated in section 3.4.1. We propose that the mechanism of J_w reduction at a certain ΔV for larger charge spreads (see section 3.4.1) is due to the reduction of the "anomalous drag" exerted on the solvent molecules by the moving ions. Further, the anomalous drag is generated due to the total reverse ionic flux, which is the sum of diffusive and electrophoretic fluxes. Therefore, the net axial osmotic flux through the pore, J_w, can be expressed as (all fluxes are in the z-direction),

$$J_w = J_w^p + J_w^{EO} + J_w^{AD} \tag{9}$$

where J_w^p is the flux generated due to the induced pressure gradient, J_w^{EO} is the electroosmotic flux due to the electric field body force, and J_w^{AD} is the flux due to anomalous drag, which contains contributions from the diffusive and electrophoretic ionic fluxes.

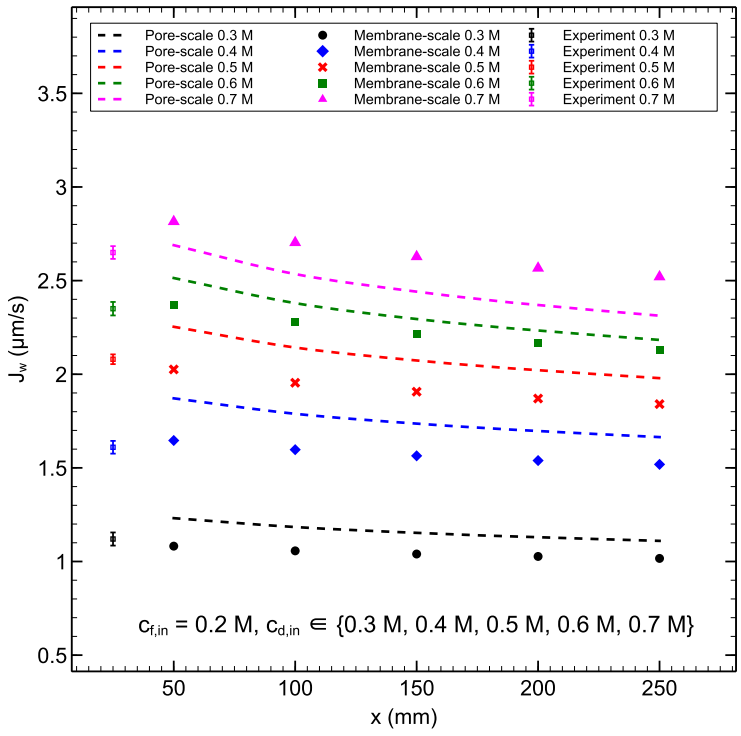

(a)

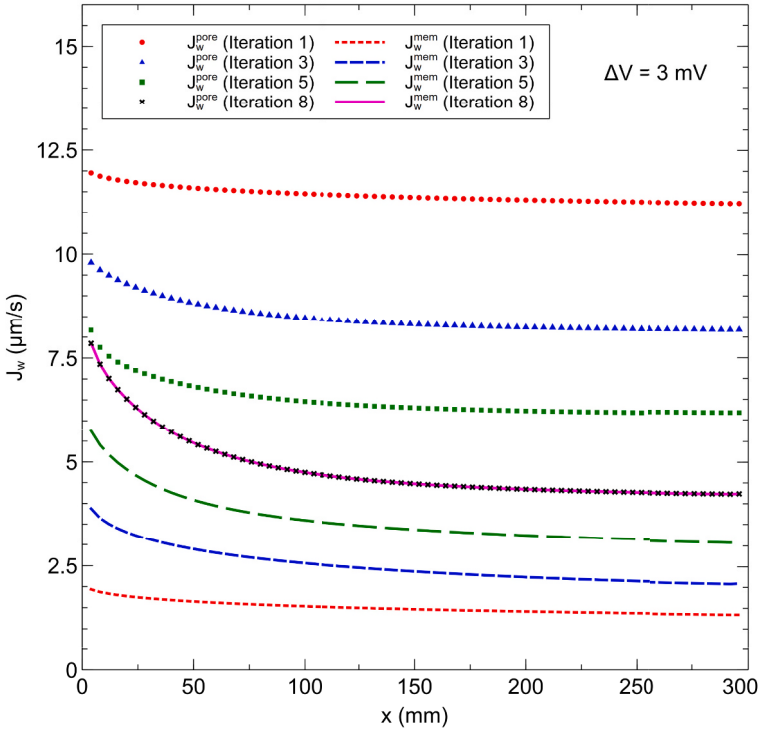

(b)

(caption on next page)

Fig. 6. Validation and demonstration of the hybrid model. x is the coordinate along the membrane. (a) A two-step validation strategy was used where the results obtained from the pore scale model were compared against the membrane-scale model at five equidistant pore positions along the membrane. Experiments were performed on our module for the baseline conditions ($\Delta V = 0$) and the corresponding J_w values for different draw concentrations were recorded on the left-side of the curves. Maximum systematic uncertainty during the experiments was calculated assuming linear error propagation and the same is indicated. Further details may be found in supplementary section S1. (b) Implementation of the hybrid model for $\Delta V = 3\,mV$ and all other parameters at the baseline level. The lines with no markers indicate J_w^{mem}, the local water flux obtained from the membrane-scale model. The markers with no lines represent J_w^{pore}, the pore-scale water flux for the 74 representative pores used in the hybrid model. The pores at the extremities of the membrane, that is, at $x = 0$, and $x = 300\,mm$, have not been included in the analysis.

3.3. Effects of varying ΔV

3.3.1. On the flow field

Understanding the dynamics of water flow in the pore is critical to developing tunable FO systems tailored to specialized applications. Since the electroneutrality condition is violated within the pore due to the presence of an EDL, the cations and anions may have different concentrations in certain regions of the pore. Therefore, the concentration distribution of the ions within the pore might be of similar interest.

Figs. 7(a)-(e) show the fluid's $u_z(z^*)$ profiles at six different radial positions in the pore. The positions are selected to present the highest contrast among the individual profiles. We observe that the flow is not fully developed throughout the pore. It is important to note that the charge is unevenly distributed on the pore wall, with a non-zero value only for $z^* \in [0.3, 0.7]$, not considering the excess spread due to smoothing, as indicated in section 2.3.4. At all radial positions except $r^* = 0.6$, the flow begins as a fully developed flow, encounters the charge spread and experiences a velocity transition (step-up or step-down), remaining fully developed throughout the charged zone. Further downstream, the flow becomes identical to the flow before encountering the charge spread. This situation is observed for all values of ΔV, irrespective of the polarity. At regions close to $r^* = 0.6$, the flow is always fully developed, indicating a balance between the electrical effects due to the wall charge, viscous effects, and the effects due to a concentration gradient across the pore. As the magnitude (absolute value) of ΔV increases, the magnitude of flow velocity at all radial positions increases due to an increased density of electric field lines, providing a stronger electroosmotic effect compared to the baseline case with $\Delta V = 0$. There are, however, some interesting changes in the nature of the flow for different values of ΔV. As evident from Fig. 7(d), at $\Delta V = 2\,mV$, the flow throughout the pore is nearly fully developed. We performed some extra simulations (not included in this study) for different distributions of $\sigma_z(z^*)$ and observed that such transition potential differences ($\Delta V_{transition}$) always exist and depend on the distribution and magnitude of $\sigma_z(z^*)$. For example, for a $\sigma_z(z^*)$ symmetric about $z^* = 0.5$, the more the charge spread, the greater was the $\Delta V_{transition}$. For negative zeta potentials, $\Delta V_{transition}$ is always positive, while for positive zeta potentials, such trends were not observed.

The flow inside the pore does not follow the typical plug-like profile characteristic of electroosmotic flows, as illustrated in Figs. 8(a)-(c), where we plot the radial variations in u_z for different locations along z. As the magnitude of ΔV is increased, the u_z profiles become increasingly parabolic in nature. It is also substantiated that the profiles are nearly identical for the pore regions before and after the wall charge spread, which is expected owing to its absence in the corresponding regions. Similar observations have been reported in [47]. Minor deviations from the parabolic shape leading to local velocity extrema are observed near the mid-section of the pore, but we expect them to be specific cases of no general significance. A possible reason for the said observation could be due to the dependence of some parts of the u_z field on zero-order Bessel functions of the first kind [47]. It is also observed that as ΔV increases in magnitude, the shapes of the axial velocity profiles tend to become decreasingly sensitive to the increase. Changes in the shapes of the profiles are barely noticeable for $|\Delta V| > 10\,mV$.

3.3.2. On concentration distribution

To know the exact distribution of the ions within the EDL, or for that matter, the entire pore, we need to calculate the concentrations of the coions and counterions throughout the modeling domain. Figs. 9(a) & 9(b) illustrate the axial variation in the ion concentrations for different radial positions in the pore, for NaCl and $MgSO_4$, respectively. The plots report variations for $\Delta V = 0$. Even if ΔV is increased to values as high as $\pm 10\,mV$, the concentration distributions for the two solutes do not change significantly. As we increase ΔV toward a more positive value, two minor but notable changes happen. Within the region of the charge spread, the slope of the straight sections of the concentration plots increases. Contrary to this trend, the slope of the linear sections outside the charge spread region decreases. Similar concentration profiles have been reported by [48] for solute concentrations of the order $10^{-4}\,M$, very different pore dimensions, and $\Delta V = 0$. As far as the radial variations in ion concentrations due to a changing ΔV are considered, there are minor effects outside the charge spread for non-zero values of ΔV, while the variations within the charge spread can essentially be ignored. In addition, we observe that the concentration split between the counterions and coions is more for NaCl compared to $MgSO_4$, especially for radial positions close to the pore axis.

The above trends can be explained to a certain extent by observing the electric field distribution in the pore. Figs. 10(a) and 10(b) show the arrow plots and streamlines for the distribution and direction of the electric field, and the 2D surface plots for the z (rainbow color theme, a & b) and r (disco color theme, a & b) components of the electric field in the pore for both NaCl and $MgSO_4$. All further observations made in this section will be for the region of the EDL effects in the baseline case ($z^* \in [0.3, 0.7]$), unless specified otherwise. For NaCl, the electric field at $r^* = 0.01$ and $z^* \sim 0.5$ is predominantly radial with a magnitude $1.55 \times 10^5 \frac{V}{m}$ for NaCl, and $-6.40 \times 10^4 \frac{V}{m}$ for $MgSO_4$. Since the magnitude of E_r for NaCl is stronger than that for $MgSO_4$ by nearly 2.5 times, the Na^+ counterions are attracted more strongly by the wall charge than Mg^{2+} coions, leading to a higher concentration asymmetry for the NaCl EDL. As we move closer to the wall, at $r^* = 0.9$, E_r is nearly constant $\forall z^* \in [0.3, 0.7]$ and valued at $2.12 \times 10^7 \frac{V}{m}$ for NaCl and $-2.37 \times 10^7 \frac{V}{m}$ for $MgSO_4$. Clearly, the difference between the E_r values for NaCl and $MgSO_4$ is not as stark as that close to the axis. Thus, as r increases, $\left|\frac{E_r^{NaCl}}{E_r^{MgSO_4}}\right|$ decreases and the relative split between the counterion and coion concentrations in NaCl and $MgSO_4$ becomes less pronounced. E_r nearly vanishes for all z outside the charged region, and so should the EDL effect of concentration asymmetry. Another look at Figs. 9(a) and 9(b) substantiates this reasoning—outside the charge spread, the concentrations of the counterions and coions are identical, irrespective of the solute used.

3.3.3. On water flux

Fig. 11 illustrates the variations in J_w obtained through the pore-scale model with ΔV. We observe that J_w increases with an increasing $|\Delta V|$ for both NaCl and $MgSO_4$. We expect a similar trend for all symmetric solutes, if not all solutes. However, due to the difference in the signs of the zeta potentials for NaCl (negative) and $MgSO_4$ (positive), the trends of an increasing J_w are opposite to each other. That is, for NaCl, for an increasingly positive ΔV, J_w increases and the direction of J_w is the

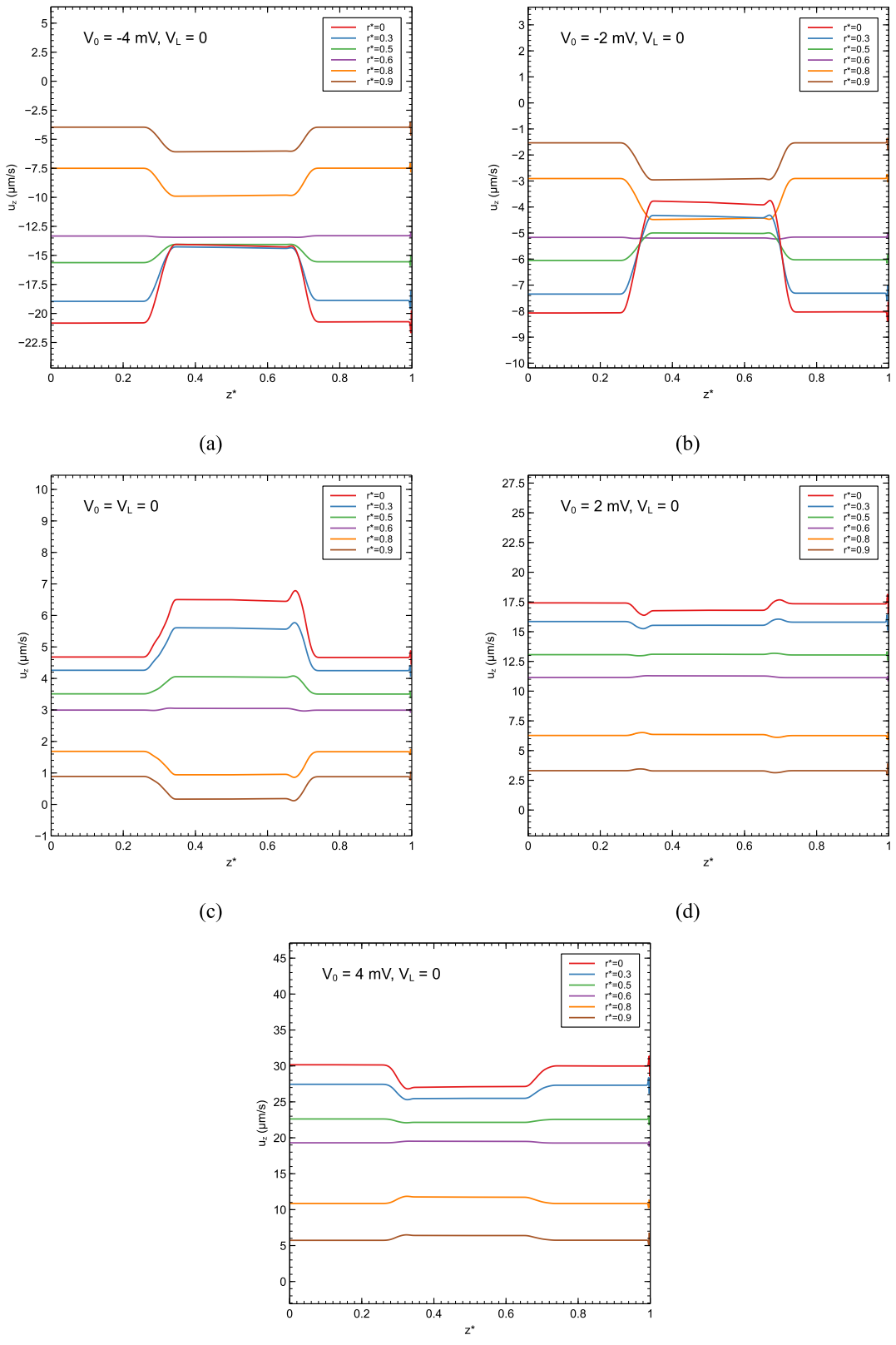

Fig. 7. $u_z(z^*)$ profiles at different radial positions within the pore. (a) $\Delta V = -4\,mV$. (b) $\Delta V = -2\,mV$. (c) $\Delta V = 0$. (d) $\Delta V = 2\,mV$. (e) $\Delta V = 4\,mV$. Conditions other than ΔV were similar to those used in the baseline model. $c_0 = 0.22\,M$, $c_L = 0.40\,M$, $\sigma_z = -0.0180\frac{C}{m^2} \forall z^* \in [0.3, 0.7]$ with smoothing. Data was reported at multiple r^* between the axis and the pore wall to provide a comprehensive representation of the hydrodynamics within the pore.

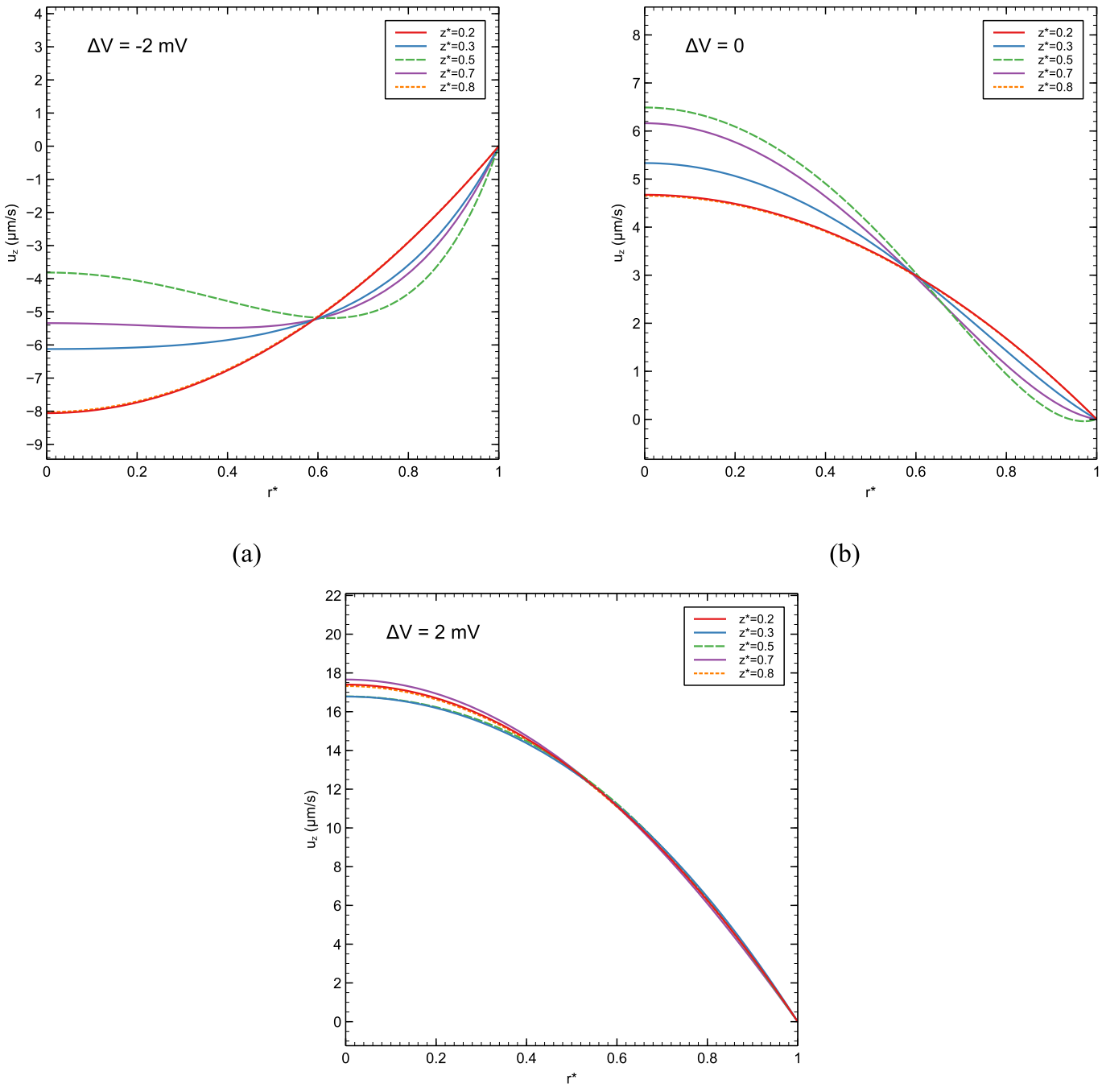

Fig. 8. $u_z(r^*)$ profiles at different axial positions along the pore. (a) $\Delta V = -2\,mV$. (b) $\Delta V = 0$. (c) $\Delta V = 2\,mV$. Conditions other than ΔV were similar to those used in the baseline model. $c_0 = 0.22\,M$, $c_L = 0.40\,M$, $\sigma_z = -0.0180\frac{C}{m^2}\forall z^* \in [0.3, 0.7]$ with smoothing. Data was reported at multiple z^* between the inlet and outlet of the pore to provide a comprehensive representation of the hydrodynamics within the pore.

same as we would expect in an identical system without the additional electric field. However, once ΔV transitions to negative values, the direction of J_w is reversed and further increases in the reverse direction as ΔV becomes increasingly negative. On the contrary, for $MgSO_4$, an increasingly negative ΔV increases J_w, which retains its natural direction (from low solute concentration to high solute concentration). As ΔV transitions to positive values, although J_w keeps increasing, the direction of J_w is reversed, and now the solvent flows from a higher solute concentration to a lower solute concentration, similar to what happens in RO. This is a rather interesting observation because it indicates that a single CMO setup can be operated both as FO and RO, with the overall flow direction dependent on the polarity of ΔV. In addition, unlike RO, no external hydraulic pressure is required in our design, and the flux direction is controlled via ΔV.From Fig. 11, we also observe a linear relationship between J_w and ΔV, given as,

$$J_w = A\Delta\Pi - \alpha_i \frac{|\sigma_z^i|}{\sigma_z^i}\Delta V \tag{10}$$

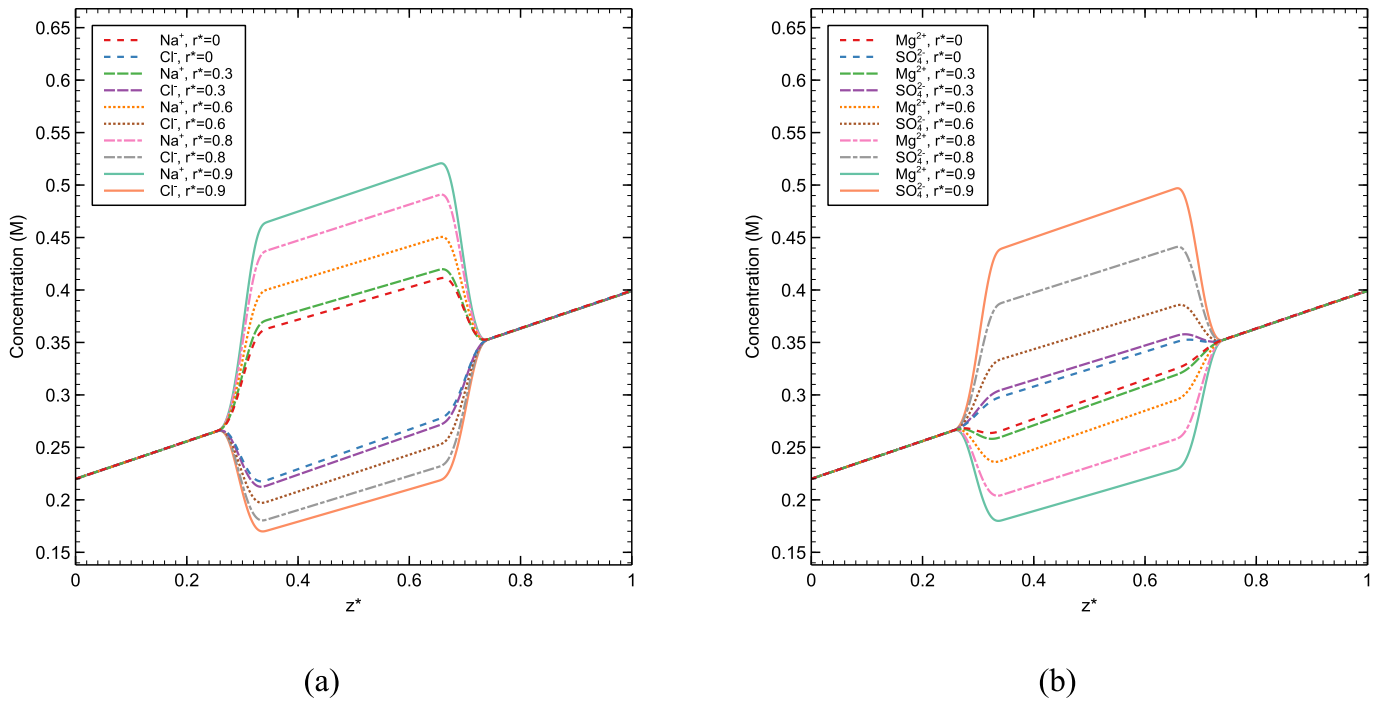

Fig. 9. Axial concentration distribution for the coions and counterions inside the pore for (a) NaCl, and (b) $MgSO_4$, for different radial positions r^* within the pore. While the magnitude of ΔV does not have substantial impact on the concentrations of the coions and counterions (see section 3.3.2), for the given case, $\Delta V = 3\,mV$ with $c_0 = 0.22\,M$, $c_L = 0.40\,M$, $\sigma_z = -0.0180\frac{C}{m^2}$ for NaCl and $\sigma_z = 0.0243\frac{C}{m^2}$ for $MgSO_4$ $\forall z^* \in [0.3, 0.7]$ with smoothing.

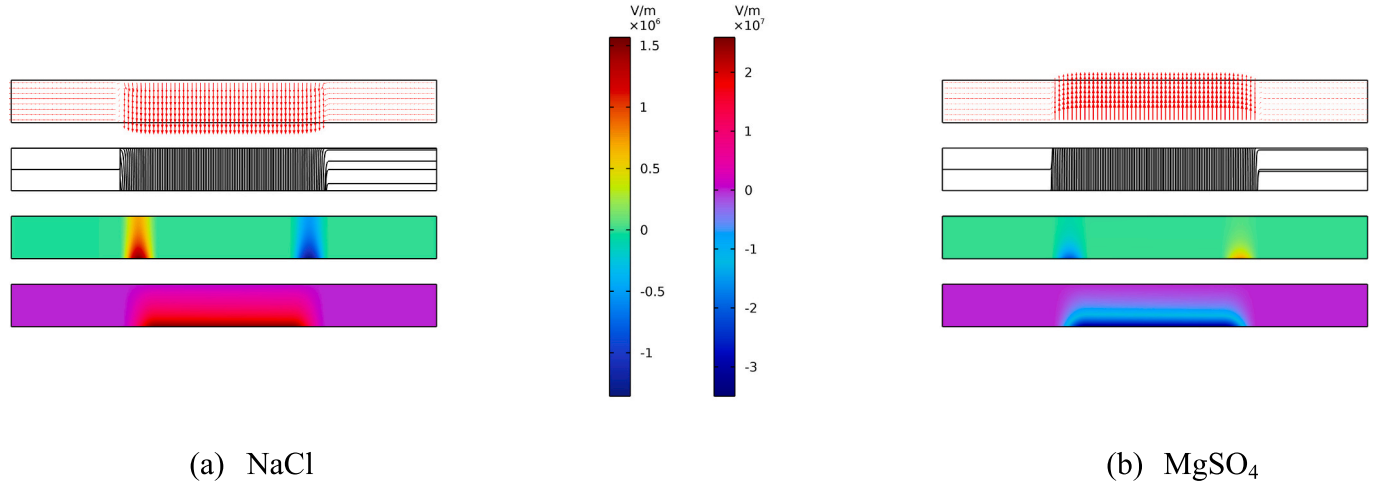

Fig. 10. Electric field distribution within the pore is visualized through arrow plots, streamlines, and surface plots for (a) NaCl and (b) $MgSO_4$. In the surface plots, E_z is illustrated with a rainbow color scheme, while E_r is depicted with a disco color scheme. Both components of electric field are measured in $\frac{V}{m}$. For the given case, $\Delta V = 3\,mV$ with $c_0 = 0.22\,M$, $c_L = 0.40\,M$, $\sigma_z = -0.0180\frac{C}{m^2}$ for NaCl and $\sigma_z = 0.0243\frac{C}{m^2}$ for $MgSO_4$ $\forall z^* \in [0.3, 0.7]$ with smoothing.

where $\Delta\Pi$ is the osmotic pressure difference across the selective layer, i can denote any symmetric electrolyte, $\alpha_{NaCl} = 3.16 \times 10^{-3}\frac{m}{V-s}$, and $\alpha_{MgSO_4} = -2.94 \times 10^{-3}\frac{m}{V-s}$. Since the chosen salts were arbitrary representatives of symmetric electrolytes, we expect Eq. 10 to be applicable for all symmetric electrolytes. However, the formula must be used with caution. The hybrid model is a nuanced and highly nonlinear system of mathematical equations, and we should not expect a straightforward relationship between α_i and various system parameters, such as pore dimensions and surface charge.

The trends observed in Fig. 11 are readily explained through Figs. 9 (a) and 9(b). Since β is close to 1 (see section 2.3.2), we know that the EDL thickness is comparable to the pore radius. This implies that the ion composition within the EDL has a significant role in determining the flow dynamics within the pore, more than for systems with $\beta \gg 1$. Figs. 9 (a) and 9(b) clearly indicate that for both NaCl and $MgSO_4$, the concentration of counterions within the EDL is more than that of the coions. Thus, as far as electroosmotic effects are concerned, for both solutes, we can state that the counterions have a higher contribution toward determining the overall flow than the coions. Additionally, as discussed in the previous section, the concentration distributions of the ions within the EDL do not demonstrate significant variations with a varying ΔV. Therefore, our statements hold true for all values of ΔV. As ΔV is increased in the positive direction, the axial electric field (E_z) is positive (except in some regions close to the charge spread) and increases throughout the pore compared to the baseline case with $\Delta V = 0$. This

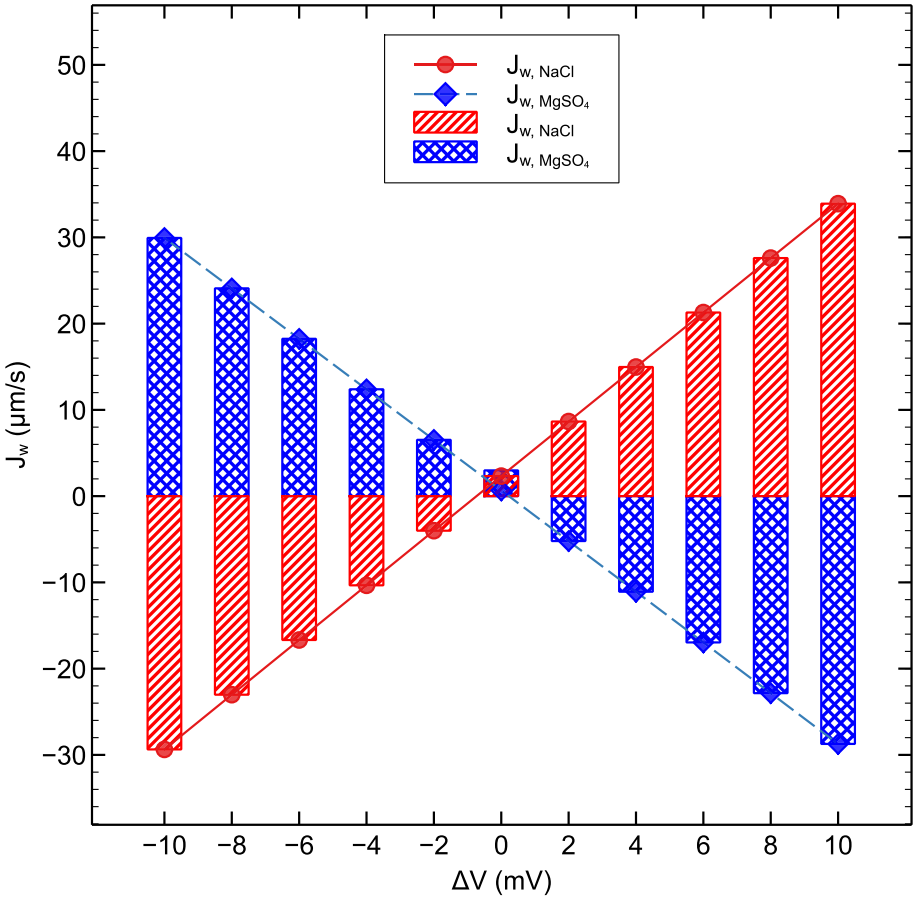

Fig. 11. Variation of J_w with changing V_0 for two symmetric electrolytes (NaCl, with $z = 1$, and $MgSO_4$, with $z = 2$). For the given case, $c_0 = 0.22\,M$, $c_L = 0.40\,M$, $\sigma_z = -0.0180\frac{C}{m^2}\forall z^* \in [0.3, 0.7]$ for NaCl, and $\sigma_z = 0.0243\frac{C}{m^2}\forall z^* \in [0.3, 0.7]$ for $MgSO_4$. Both surface charge spreads are smoothened at the ends of their extents as described in section 2.3.4.

implies that a greater axial force will be exerted on the counterions and coions compared than that exerted for $\Delta V = 0$. Since the counterions are positive for NaCl and negative for $MgSO_4$, with an increasingly positive ΔV, they tend to drive the solvent in the positive direction for NaCl, and the negative direction for $MgSO_4$. The flow rate, and thus J_w, increases with an increase in ΔV and the consequently higher driving force, regardless of the direction of the overall flow.

From section 3.2, we know that the total flux is not simply determined by E_z, but also the pressure gradient and the anomalous drag flux components. In the present case for NaCl, with increasing ΔV values, $\frac{\partial p}{\partial z}$ values become less negative, reducing $|J_w^p|$. Somewhere within $4\,mV < \Delta V < 6\,mV$, $\frac{\partial p}{\partial z}$ becomes positive and actively opposes a forward J_w. Expectedly, J_w^{AD} is always negative for all ΔV, but becomes less negative with increasing ΔV, effectively supporting the forward J_w. Thus, we can say that an increase in J_w with an increasing ΔV is observed due to the forward J_w promotion by J_w^{EO} and J_w^{AD} overpowering an active opposition by J_w^p. A similar discussion may be extended to $MgSO_4$.

Drawing the corresponding $MgSO_4$ parallels from different physical effects observed in NaCl is facile. Hence, in further sections, we analyze the case of NaCl only.

3.4. Effects of varying the wall charge distribution

Most studies on membrane transport present the wall surface charge as a single, constant value for diverse system conditions. However, there is no reason to assume that the charge must be uniform in either distribution or magnitude, as suggested in several scholarly works through their axial electric potential plots [81,82]. In this section, we investigate how changes in the charge spread influence J_w. This is done by adopting a two-step approach. First, while assuming a constant $\sigma_z(z^*)$ symmetric about $z^* = 0.5$, we vary its extent from 20% of L_{pore} to 80% of L_{pore}. Next, it is noteworthy that the charge spread may not necessarily be symmetric about $z^* = 0.5$, hence we assess the effects of an asymmetric charge spread centered at varying z and spanning 20% of L_{pore}.

3.4.1. Effects of the changing extent of charge spread symmetric about $z^* = 0.5$.

Several interesting flow phenomena can be observed within the pore on varying the extent of the symmetric charge spread at different ΔV. First, we explore the effects on J_w, which are illustrated in Fig. 12(a). Although the linear dependence of J_w on ΔV is maintained for all charge spreads, things are not straightforward while identifying the trends in J_w variations with a changing charge spread. From Fig. 12(a), we can see that as the charge spread is increased from 20% to 80%, J_w becomes more sensitive to changes in ΔV. For example, for every unit mV increase in ΔV, J_w increases by $1.59\frac{\mu m}{s}$ for a 20% charge spread. This is in contrast with the $6.47\frac{\mu m}{s}$ increase in J_w per unit mV for an 80% charge spread. Ordinarily, increasing the charge spread would mean an increased number of counterions for a larger region of the pore. Subject to a favorable electric field and the consequent driving force, J_w may be expected to increase in the osmosis direction, as discussed in the previous section. Instead, the J_w first increases to a maximum and then decreases. This confirms the existence of competing flow drivers affected by a changing charge spread (refer to section 3.2 on mechanism of osmosis), the details of which are presented here.

For any ΔV, the z pressure gradient, $\frac{\partial p}{\partial z}$, within the EDL is generally

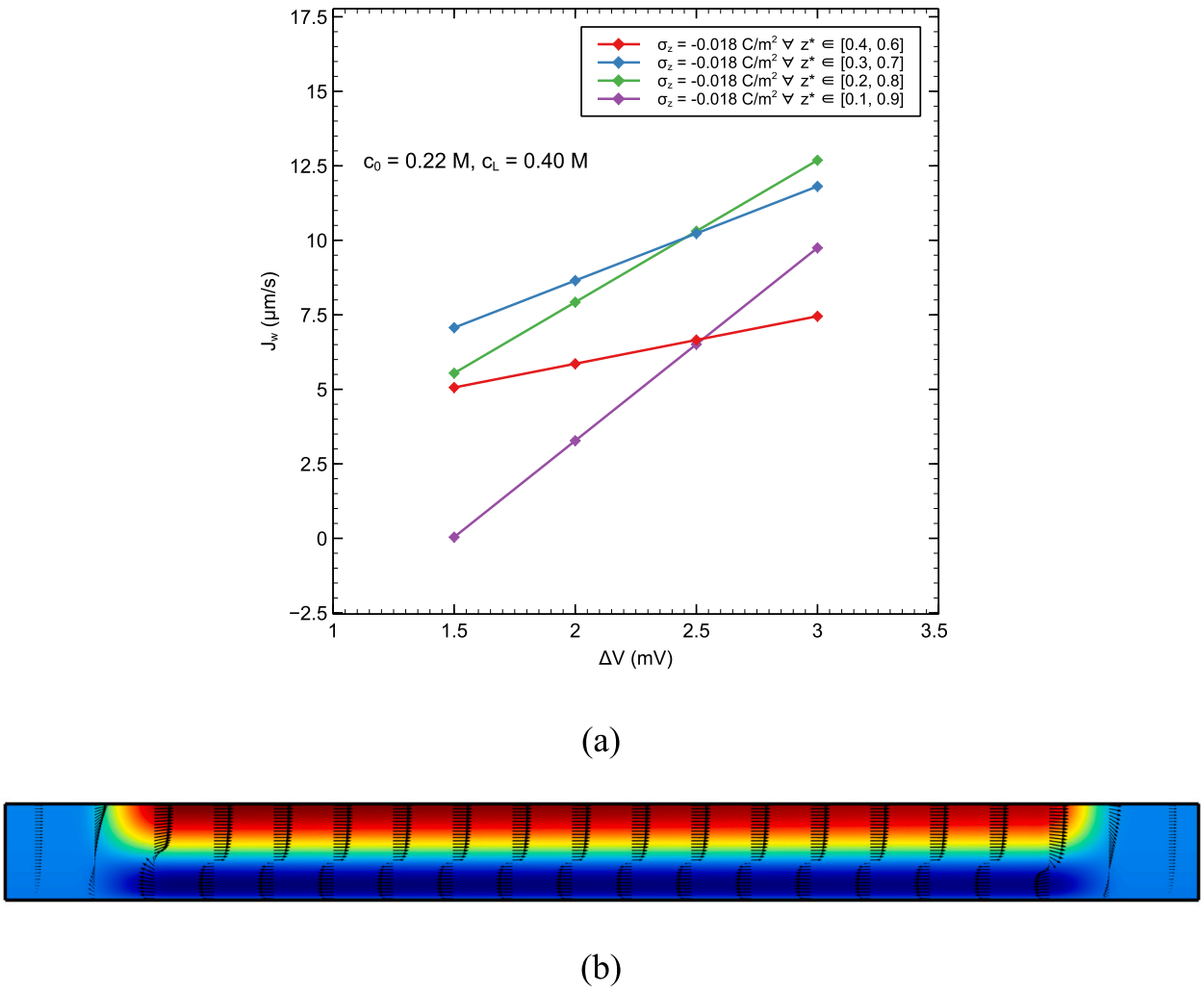

Fig. 12. Effects of a changing charge spread. (a) Variation of J_w with changing ΔV and different extents of charge spread centered around $z^* = 0.5$, ranging from 20% to 80%. (b) A recirculation pump is observed within the pore for $\Delta V = 1.5\,mV$ and an 80% charge spread. For all cases, $c_0 = 0.22\,M, c_L = 0.40\,M$ NaCl along with other details as mentioned when required.

negative and its magnitude increases as the extent of the charge spread increases. For example, with $\Delta V = 1.5\,mV$, for a 40% charge spread, $\frac{\partial p}{\partial z}$ within the EDL is around $-17.84\frac{Pa}{\text{Å}}$, and for an 80% charge spread, $\frac{\partial p}{\partial z}$ is nearly $-30.70\frac{Pa}{\text{Å}}$, implying an increase in $|J_w^p|$. These observations imply that the induced hydrodynamic pressure gradient tends to maintain the net osmotic flow in the positive z direction.

Now, we shift our attention to the body force on the EDL ions generated due to ΔV (electroosmotic effect). For a 20% charge spread, we observe that E_z within the EDL is predominantly positive for all z and ΔV and enhances the osmotic flow in the positive z direction. However, as the charge spread increases, E_z becomes negative, likely due to the large extent of the negative wall charge which introduces a strong negative E_z in the EDL. Within the EDL, E_z is increasingly negative as we move toward the pore wall. For a negative E_z, the counterions for NaCl will be driven in the negative z direction, and since the number of counterions exceeds the coions in the EDL, we can expect the electroosmotic flow to have a retarding effect on the overall forward J_w.

J_w^{AD} is always negative for all charge spreads and its magnitude determines the retarding anomalous drag. We observe that $|J_w^{AD}|$ nominally decreases when the charge spread increases from 20% to 40%, and keeps increasing for higher charge spreads. This indicates that increasing the extent of charge spread from 40% retards the osmotic flow in the positive z direction. We observe this effect at all radial positions. Notably, for $\Delta V = 1.5\,mV$, this effect is especially pronounced in regions close to the pore wall, compared to radial positions nearer to the axis. As the charge spread increases, near the wall, coupled with the retarding electroosmotic flux, $J_w^{AD} + J_w^{EO}$ becomes more negative than J_w^p, and J_w is observed in the negative z-direction. Since J_w is positive away from the wall, we effectively have a recirculation pump within the pore, where the fluid recirculates in the region of the EDL and J_w through the pore is nearly zero, as illustrated in Fig. 12(b). Given the no slip boundary condition on the wall, u_z crossing zero and becoming negative as we move from the axis to the wall implies the existence of two extrema, one positive near the axis, and one negative near the wall. This is an intriguing observation and may have widespread applications. For example, microarray assays often require mixing of samples of small molecules like DNA and specific antigens and their kinetics are limited by the rate of diffusive mixing [83]. Special devices like nanomixers are often employed to achieve a desired level of mixing [83]. A precision-tuned CMO system may help overcome mixing limitations by promoting osmotic recirculation within the nanochannel, provided that the channel walls acquire charge upon contact with the electrolyte.

We can also take a look at the concentration distribution of the ions within the pore, although it follows predictable trends. As shown in Fig. 13, the trends in the split between the counterion and coion concentrations are quite similar to what were observed in section 3.3.2. The concentrations are plotted for $r^* = 0.8$. Increasing the charge spread

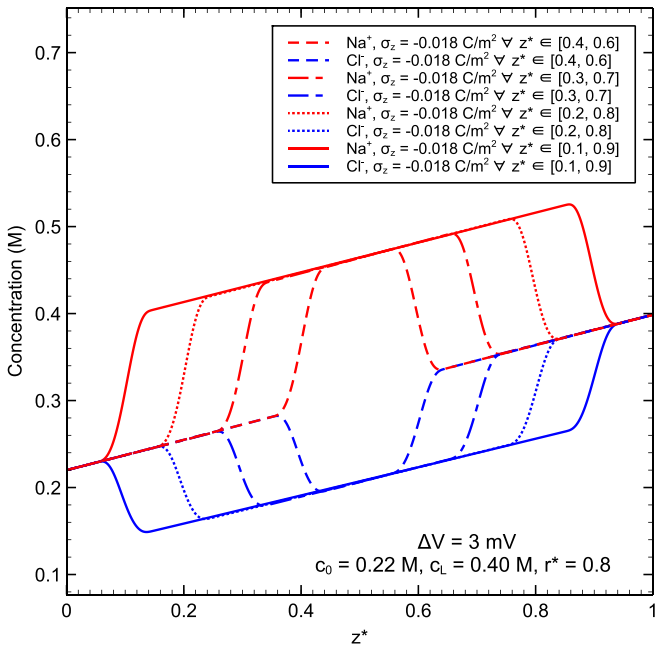

Fig. 13. Concentrations of coions ($Cl^-, c_b(z^*)$) and counterions ($Na^+, c_a(z^*)$) for different extents of charge spread centered around $z^* = 0.5$ at $r^* = 0.8$. For the current case, $c_0 = 0.22\,M$, $c_L = 0.40\,M$, and $\Delta V = 3\,mV$.

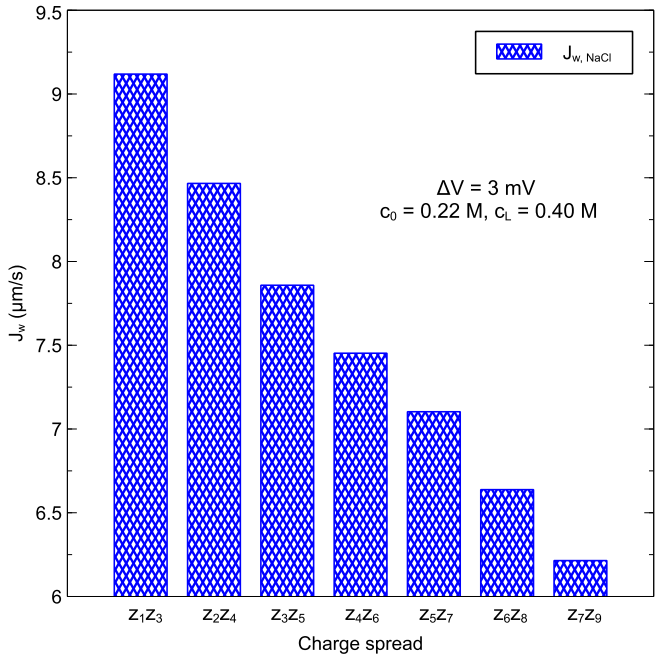

Fig. 14. Reduction in J_w with an increasing distance of the 20% charge spread from the inlet of the pore. $z_i z_{i+2} \forall i \in \{1, 2, \ldots\ldots, 7\}$ implies that the charge is uniformly localized in $\frac{i}{10} \leq z^* \leq \frac{i+2}{10}$ For the current case, $c_0 = 0.22\,M$, $c_L = 0.40\,M$, and $\Delta V = 3\,mV$.

merely extends the influence of the EDL effects and has no special influence on the magnitude of the split. Interestingly, the concentrations of the counterions and coions within the EDL lie in the envelop defined by the extents of the concentration asymmetry about $c = 0.18\,z^* + 0.22$, where c is in M.

3.4.2. *Effects of the changing location of charge spread with a 20% extent*

We discussed that there seems to be no reason for the surface charge to be uniformly distributed along the length of the pore in section 2.3.1.1. Since we considered a symmetric distribution of surface charge on the pore wall about $z^* = 0.5$, it is also necessary to discuss the cases where the surface charge is not symmetric about $z^* = 0.5$, but localized in a certain region of the pore with a consistent spread. We first investigate the variations in J_w with a changing localization of surface charge along the pore length, as shown in Fig. 14. For a charge spread with a 20% extent, we observe that the farther the spread from the inlet of the pore, the lower the overall J_w obtained through the pore. Again, we follow the approach outlined in section 3.2 and look at each of the component fluxes within J_w. First, to understand the variation in J_w^p, we look at $\frac{\partial p}{\partial z}$. $\frac{\partial p}{\partial z}$ can be analyzed against the backdrop of two regions along the z-direction—within the EDL and outside the EDL. We observe that $\frac{\partial p}{\partial z}$ is negative both before and after the EDL region and becomes less negative as the charge spread moves farther from the inlet. For example, $\frac{\partial p}{\partial z}$ outside the EDL is $\sim -10\,\frac{Pa}{\text{Å}}$ for a charge spread between $z^* = 0.1$ and $z^* = 0.3$ and $\sim -7\,\frac{Pa}{\text{Å}}$ for a charge spread between $z^* = 0.7$ and $z^* = 0.9$. In addition, $\frac{\partial p}{\partial z}$ tends to stay positive (initially negative, becomes positive as charge spread is shifted away from the inlet) throughout the EDL and appears to increase and saturate as the charge is localized farther from the pore inlet. Thus, as the charge moves away from the inlet, owing to an decrease in J_w^p, the overall J_w in the z-direction tends to decrease and remain constant.

E_z is always positive within the EDL and increases ever so slightly as the charge is located away from the inlet. Thus, if the primary driver of the overall flow were J_w^{EO}, J_w should have increased as the charge is moved toward the outlet. From Fig. 14, we can observe that this is not the case, and therefore, the factor responsible for retarding the overall flow must be something other than J_w^{EO}. Clear differences between the J_w for different charge locations are observed when we investigate J_w^{AD}. J_w^{AD} becomes increasingly negative as the charge moves closer to the pore outlet, and along with the trends in J_w^p, this explains the corresponding reduction in J_w.

An intriguing observation can be made if the plots for the ionic concentrations for the 80% extent symmetric and 20% extent asym-

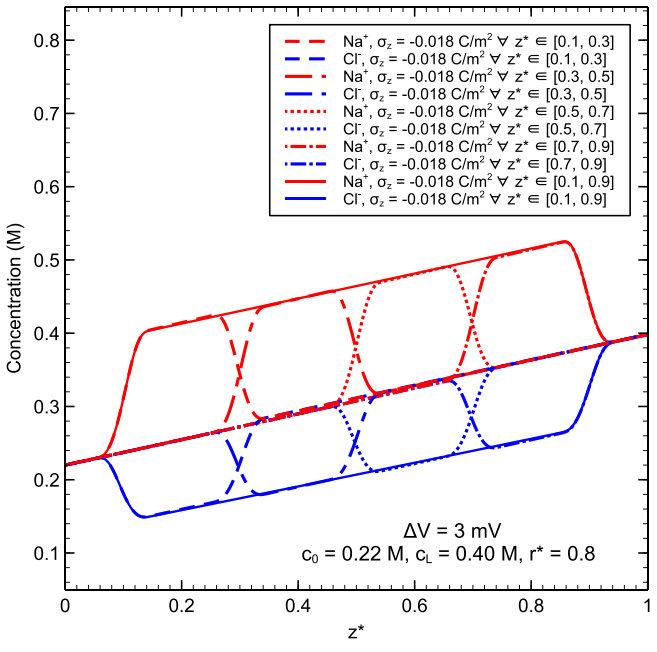

Fig. 15. Concentrations of coions ($Cl^-, c_b(z^*)$) and counterions ($Na^+, c_a(z^*)$) for different localizations of 20% charge spread centered as indicated. All values have been reported for $r^* = 0.8$. For the current case, $c_0 = 0.22\,M$, $c_L = 0.40\,M$, and $\Delta V = 3\,mV$.

metric charge spreads are superimposed, as shown in Fig. 15. We observe that the magnitude of concentration split between the counterions and coions for the asymmetric spreads is identical to the symmetric spread regardless of the position of the asymmetric spread. Therefore, the ionic concentration distribution profiles within the EDL for a symmetric charge spread with constant charge density are similar to those obtained for an asymmetric charge spread with constant charge density. While the shape and magnitude of concentration split are similar for both the symmetric and asymmetric cases, the axial extent of concentration split is identical to the extent of axial region with a non-zero surface charge density. We also notice that the ionic concentration distributions for a charge spread with a charge density profile similar to a step function (without smoothing) can be expressed as a linear superposition of the concentration profiles in a transformed coordinate system obtained for any constituent charge distributions with step function charge spreads. The transformed coordinates $(z^{\#}, c^{\#})$ are related to the original coordinates through the following matrix transformation,

$$\begin{bmatrix} z^{\#} \\ c^{\#} \end{bmatrix} = \begin{bmatrix} c - c_0 & z \\ -z & c - c_0 \end{bmatrix} \begin{bmatrix} \sin\theta \\ \cos\theta \end{bmatrix} \tag{11}$$

where z and c refer to the original x and y coordinates in Fig. 15, and $\tan\theta = \frac{c_L - c_0}{L_{pore}}$ (in $\frac{M}{\text{Å}}$).

3.5. Effects of changing the selective layer thickness

With our assumption of straight cylindrical pores, the selective layer thickness is indicated by the pore length L_{pore}. In Fig. 16, we illustrate the variation in $\ln(J_w)$ with $\ln(L_{pore})$ for different values of ΔV. Decreasing linear trends in Fig. 16 indicate a hyperbolic relationship between J_w and L_{pore}. As ΔV is increased, the curves become increasingly closer to each other, likely indicating the existence of a theoretical saturation voltage ΔV_{sat}, beyond which increasing ΔV produces insignificant gains in J_w for any L_{pore}. However, this remark must be interpreted with caution, as increasing ΔV to values as high as ΔV_{sat} may produce other physical effects that compete with the increase in J_w obtained by

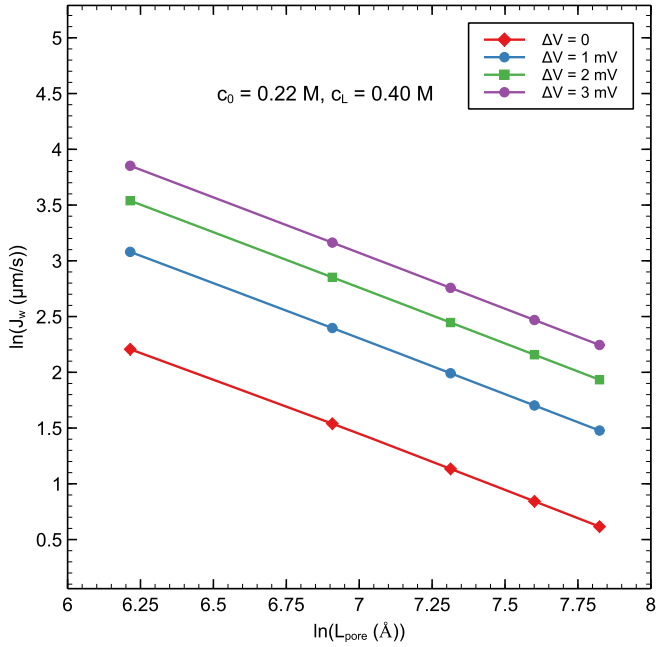

Fig. 16. Variation of $\ln(J_w)$ with changing $\ln(L_{pore})$ for $\Delta V \in \{0, 1, 2, 3\}\, mV$. Other simulation conditions are $c_0 = 0.22\,\text{M}$, $c_L = 0.40\,M$, $\sigma_z = -0.0180 \frac{C}{m^2} \forall z^* \in [0.3, 0.7]$.

increasing ΔV. From Fig. 16, we can roughly write the following semi-empirical relationship,

$$J_w L_{pore} = f\left(c_0, c_L, R_{pore}, \sigma_z(z^*)\right) + g\left(c_0, c_L, R_{pore}, \sigma_z(z^*)\right)\left(\frac{\Delta V}{\Delta V_{sat}}\right) \tag{12}$$

where, $0 \le \Delta V \le \Delta V_{sat}$, and for our baseline case, $f\left(c_0, c_L, R_{pore}, \sigma_z(z^*)\right) = 4258.2 \frac{(\mu m - \text{Å})}{s}$ and $g\left(c_0, c_L, R_{pore}, \sigma_z(z^*)\right) = 6377.8 \frac{(\mu m - \text{Å})}{s}$.

From our analysis, we can conclude that in the absence of competing effects like structural relaxation, hydrophilicity, inhomogeneity, to name a few, the thinner the polyamide selective layer in a uniformly dense TFC membrane for membrane desalination applications, the better the water recovery. Conventional solute-diffusion approaches for explaining variations in J_w with a changing selective layer thickness attribute this observation to a reduction in mass transfer resistance due to a thinner selective layer, among other contributors [38,64,84]. Extending a similar discussion to the reverse salt flux, we can expect thinner selective layers to offer little resistance to reverse salt flux, that is, a lower selectivity. Thus, thin selective layers typically offer higher water permeability but may compromise selectivity [64].

We can explain these observations through the paradigm developed in section 3.2. For a specific ΔV, as L_{pore} increases, the magnitude of $\frac{\partial p}{\partial z}$ decreases. Although the pressure gradient is always favorable to flow in the positive z-direction, a reduction in $\left|\frac{\partial p}{\partial z}\right|$ with an increasing L_{pore} implies a decrease in J_w^p, which contributes to a reduction in J_w. As L_{pore} increases, the magnitude of E_z within the EDL decreases, regardless of its direction (E_z is negative for $\Delta V = 0$ and $\Delta V = 1\,mV$ and positive otherwise). Thus, for $\Delta V = 0$ and $1\,mV$, increasing L_{pore} reduces the retarding effect of J_w^{EO}, effecting an increase in J_w. For $\Delta V = 2$ and $3\,mV$, increasing L_{pore} reduces the E_z, and consequently, J_w^{EO}, thereby reducing J_w. For a complete picture of J_w reduction with an increasing L_{pore}, we must investigate the trends in J_w^{AD}. We find that the magnitude of J_w^{AD} and hence the anomalous drag experiences significant reduction as L_{pore} in increased. For example, as L_{pore} is increased from 500 Å to 2500 Å, J_w^{AD} reduces from $-13.61 \frac{mol}{m^2 - s}$ to $-2.74 \frac{mol}{m^2 - s}$. Interestingly, J_w^{AD} is also related to L_{pore} in a hyperbolic form and does not demonstrate significant variation with ΔV. Thus, we predict a relationship of the form $J_w^{AD} L_{pore} = f^*\left(c_0, c_L, R_{pore}, \sigma_z(z^*)\right)$, with J_w^{AD} always negative. Therefore, increasing L_{pore} promotes the positive contribution of J_w^{AD} to the forward J_w.

From the premise of the preceding discussion, we infer that the primary mechanism responsible for the reduction in J_w with an increasing L_{pore} is a decrease in the magnitude of the axial pressure gradient $\frac{\partial p}{\partial z}$ overpowering the forward J_w promotion effects due to J_w^{EO} and J_w^{AD}. Investigating the effects of changing L_{pore} on the ionic concentration distributions within the EDL yields ubiquitous results with the profiles for counterion and coion concentrations plotted against z^* being identical for all values of L_{pore}.

4. Conclusions

Forward Osmosis (FO) has tremendous potential for wastewater concentration and treatment, ultimately leading to zero/minimal liquid discharge. However, a low water flux is often a challenging barrier to FO's viability in commercial-scale wastewater management. In this work, we introduce the concept of capacitive multi-osmosis (CMO) as a means to enhance forward osmosis (FO) performance through a non-contact electric field. For performance assessment, we developed a hybrid-scale modeling approach that couples the capabilities of membrane-scale and pore-scale CFD models to capture the concentration polarization (CP) phenomena in the system, along with the electrokinetic phenomena observable within the selective layer once the

system is subject to external electric fields. Our model reveals that appropriately applied non-contact external electric fields can effectively augment the CMO water flux, where both the magnitude and polarity of the electric field govern the direction and extent of water transport in the system. For representative CMO systems utilizing symmetric electrolytes such as NaCl and $MgSO_4$ as the feed and draw solutions, a potential difference of a few hundred volts across the system can yield a substantial enhancement in the water recovery. For example, as evident from Fig. 6(b), for $\Delta V = 3\,mV$ (equivalent to 178.29 V across the system), we observe a three-fold increase in the system water flux, contrary to the nearly six-fold increase predicted for the pore-scale water flux in Fig. 11. This difference arises because the hybrid model adequately captures the membrane-scale phenomena of internal and external CP and adjusts the pore-scale water flux accordingly.

Beyond quantifying performance, our model provides new physical insights into the multifaceted nature of osmosis under an electric field, showing it to arise from a delicate interplay between hydrodynamic, electroosmotic, electrophoretic, and diffusive mechanisms that may act synergistically or antagonistically depending on the CMO system configuration.

Parametric analyses reveal several noteworthy trends. For instance, increasing ΔV under a fixed set of system parameters leads to a nearly linear increase in J_w for CMO systems utilizing identical symmetric electrolytes as the feed and draw solutions. Moreover, varying the wall charge extent around $z^* = 0.5$ indicated the existence of a critical $\Delta V = 1.5\,mV$, which turned the pore channel into a recirculation pump at 80% charge spread. This phenomenon suggests the potential to harness CMO systems as electrically-driven nanomixers enabling enhanced mixing in confined environments where conventional mixing is otherwise limited. We also observed that regardless of the wall charge extent, the axial concentration curves of the ions lie within an envelope defined by the extents of the concentration asymmetry about a straight line between c and z^*. We also propose a semi-empirical hyperbolic correlation between J_w and the selective layer thickness, indicating that thinner selective layers favor permeability at the expense of selectivity.

Overall, our work establishes a fundamental framework to interpret and predict electric-assisted osmotic transport, paving the way for rational design and optimization of next-generation CMO systems for water recovery and reuse.

5. Limitations and future work

Our current work is developed to establish the theoretical basis of capacitive multi-osmosis (CMO) and therefore incorporates several simplifying assumptions. The feed and draw solutions we used were uncontaminated solutions of symmetric salts like NaCl and $MgSO_4$. However, real wastewater may contain several other components in addition to inorganic ions, such as organic matter, biological components, micropollutants, heavy metal complexes, and dissolved gases. While several of these contaminants may have minor or indirect effects on the osmotic pressure profile of the feed and draw solutions, they may also influence the CMO process in other ways, such as pH alteration, fouling, and membrane interactions. The current model can be expanded to deal with such effects. For instance, compositional effects may be integrated into the hybrid model as osmotic coefficients, activity corrections, and distinct thermophysical property variations within the model. Miscellaneous wastewaters can be modeled using the Maxwell-Stefan framework, incorporating the appropriate thermodynamic factors through software or experiments.

While the current modeling strategy works well for symmetric ionic electrolytes, systems with other predominant solute-membrane interactions, such as steric, Donnan, and dielectric, can be modeled using an extended form of the Nernst-Planck equations, as in [56]. Similarly, for highly concentrated draw solutions, ion–ion interactions and species friction may invalidate the continuum assumptions, which is likely to define a solute concentration limit to be addressed in future studies. In addition, the evaluation of CMO here assumes the validity of continuum physics, which may be contentious given the dimensions of our numerical domain (see section 2.3.6). Although we discuss this in supplementary section S7, future work may bridge continuum and molecular-scale descriptions.

Once we validated the pore-scale model against the baseline membrane-scale model and experiments, the concentrations at the pore's inlet and outlet were fixed to reflect the CPs observable for an FO system without electric field. When the system was subjected to an external electric field, J_w was found to increase. Since the effects of an increased ICP were not considered while exploring pore-scale electrokinetics, the increased flux does not reflect the overall CMO flux. Similar to the demonstration of calculations of the overall CMO flux for $\Delta V = 3\,mV$ in section 3.1, future studies may use the hybrid algorithm to simultaneously solve the pore and membrane-scales, accommodate the effects of ICP, and obtain the performance of the entire CMO module for all ΔV and other pore parameters used in the present work.

Finally, we plan to fabricate the CMO system and assess its performance under various configurations. A pore network model built on the current foundation and 3D membrane reconstruction will be essential for realistic data generation.

Essentially, the current study is focused on developing the concept of capacitive multi-osmosis, and the hybrid model intends to explore an interpretable element of the entire system. This helps isolate key physical phenomena governing the characteristics of the CMO system and provides critical insights for the potential scale-up of OMSPs and future development of CMO as a paradigm.

Nomenclature

Roman letters

A	$m^2\ s\ kg^{-1}$	Pure water permeability of the selective layer
c_0	M	Concentration at the pore inlet
c_L	M	Concentration at the pore outlet
$c_{f,in}$	M	Feed inlet concentration
$c_{d,in}$	M	Draw inlet concentration
c_i	M	Concentration of cation $(i = a)$ or anion $(i = b)$
$\bar{c}$	M	Mean solute concentration in the pore
D_i	$m^2\ s^{-1}$	Diffusion coefficient of cation $(i = a)$ or anion $(i = b)$ in aqueous solution
e	C	Electronic charge $\left(1.602 \times 10^{-19}\ C\right)$
F	$C\ mol^{-1}$	Faraday constant $\left(96485.33 \frac{C}{mol}\right)$
J_w	$\mu m\ s^{-1}$	Water flux
J_w^{pore}	$\mu m\ s^{-1}$	Mean pore-scale flux
J_w^{mem}	$\mu m\ s^{-1}$	Mean membrane-scale flux
J_w^{P}	$\mu m\ s^{-1}$	Water flux component due to induced pressure gradient
J_w^{EO}	$\mu m\ s^{-1}$	Water flux component due to electroosmotic forces
J_w^{AD}	$\mu m\ s^{-1}$	Water flux component due to anomalous drag
k_B	$J\ K^{-1}$	Boltzmann constant $\left(1.381 \times 10^{-23} \frac{J}{K}\right)$
L	mm	Length of the CMO module
L_{pore}	Å	Length of the pore
MN	–	Mesh number
N_A	mol^{-1}	Avogadro constant $\left(6.0221 \times 10^{23}\ mol^{-1}\right)$
p_0	bar	Pressure at the pore inlet
TOL	–	Convergence tolerance $\left(10^{-6}\right)$
r	Å	Radial coordinate of the pore
r^*	–	Dimensionless radial coordinate $\left(\frac{r}{R_{pore}}\right)$
R_{pore}	Å	Radius of the pore
T	K	Temperature $(298.15\ K)$
t_{PSL}	μm	Support layer thickness
$t_{c,f}$	mm	Feed channel thickness
$t_{c,d}$	mm	Draw channel thickness
$u_{f,in}$	$m\ s^{-1}$	Feed inlet speed
$u_{d,in}$	$m\ s^{-1}$	Draw inlet speed

(*continued on next page*)

(*continued*)

V_0	mV	Electric potential at pore inlet
V_L	mV	Electric potential at pore outlet
ΔV	mV	Electric potential difference across the selective layer
ΔV_{mod}	V	Electric potential difference across the CMO module
$\Delta V_{transition}$	mV	Electric potential difference for transition to fully-developed fluid flow
z	Å	Axial coordinate of the pore
z^*	–	Dimensionless axial coordinate $\left(\frac{z}{L_{pore}}\right)$
z_i	–	Charge on cation $(i = a)$ or anion $(i = b)$

Greek letters

α_i	$m\,V^{-1}\,s^{-1}$	Linearity coefficient (i can represent any symmetric solute, see Eq. 10)
β	–	Electrokinetic parameter
ε	–	Support layer porosity
ϵ	$C^2\,kg^{-1}\,m^{-3}\,s^{-2}$	Permittivity of the medium
κ	m^2	Pure water permeability of the support layer
ω	–	Valency of ions in a symmetric solute
$\Delta\Pi$	bar	Osmotic pressure difference across the selective layer
Φ	V	Electric potential
ρ	$kg\,m^{-3}$	Mass density of the fluid
ρ_v	$C\,m^{-3}$	Volumetric space charge density
σ_z	$C\,m^{-2}$	Pore surface charge distribution
τ	–	Support layer tortuosity
ζ_0	mV	Zeta potential

CRediT authorship contribution statement

Shivang Rampriyan: Writing – review & editing, Writing – original draft, Visualization, Validation, Methodology, Investigation, Formal analysis, Conceptualization. **Bahni Ray:** Writing – review & editing, Supervision, Project administration, Funding acquisition, Conceptualization. **Bijoy Bera:** Writing – review & editing, Supervision, Project administration, Investigation, Funding acquisition, Formal analysis, Conceptualization.

Declaration of competing interest

The authors declare that they have no known competing financial interests or personal relationships that could have appeared to influence the work reported in this paper.

Acknowledgment

The authors thank the Multi-institute faculty interdisciplinary project (MFIRP) between IIT Delhi and TU Delft for funding the research. SR acknowledges the funding and support from Prime Minister's Research Fellowship (PMRF) awarded by the Ministry of Education, Government of India.

Appendix A. Supplementary data

Supplementary data to this article can be found online at https://doi.org/10.1016/j.cej.2026.172935.

Data availability

Data will be made available on request.

References

[1] E.R. Jones, M.T.H. Van Vliet, M. Qadir, M.F.P. Bierkens, Country-level and gridded estimates of wastewater production, collection, treatment and reuse, Earth Syst. Sci. Data. 13 (2021) 237–254, https://doi.org/10.5194/essd-13-237-2021.
[2] A. Panagopoulos, K.J. Haralambous, M. Loizidou, Desalination brine disposal methods and treatment technologies - a review, Sci. Total Environ. 693 (2019) 133545, https://doi.org/10.1016/j.scitotenv.2019.07.351.
[3] A. Neilly, V. Jegatheesan, L. Shu, Evaluating the potential for zero discharge from reverse osmosis desalination using integrated processes - a review, Desalin. Water Treat. 11 (2009) 58–65, https://doi.org/10.5004/dwt.2009.843.
[4] J. Rioyo, V. Aravinthan, J. Bundschuh, M. Lynch, A review of strategies for RO brine minimization in inland desalination plants, Desalin. Water Treat. 90 (2017) 110–123, https://doi.org/10.5004/dwt.2017.21439.
[5] K.Y. Toh, Y.Y. Liang, W.J. Lau, G.A. Fimbres Weihs, A review of CFD modelling and performance metrics for osmotic membrane processes, Membranes (Basel). 10 (2020) 1–30, https://doi.org/10.3390/membranes10100285.
[6] W.Y. Chia, S.R. Chia, K.S. Khoo, K.W. Chew, P.L. Show, Sustainable membrane technology for resource recovery from wastewater: forward osmosis and pressure retarded osmosis, J. Water Process Eng. 39 (2021) 101758, https://doi.org/10.1016/j.jwpe.2020.101758.
[7] F.E. Ahmed, A. Khalil, N. Hilal, Emerging desalination technologies: current status, challenges and future trends, Desalination 517 (2021) 115183, https://doi.org/10.1016/j.desal.2021.115183.
[8] M. Mohammadifakhr, J. de Grooth, H.D.W. Roesink, A.J.B. Kemperman, Forward osmosis: a critical review, Processes 8 (2020) 404, https://doi.org/10.3390/PR8040404.
[9] Y. Xu, X. Peng, C.Y. Tang, Q.S. Fu, S. Nie, Effect of draw solution concentration and operating conditions on forward osmosis and pressure retarded osmosis performance in a spiral wound module, J. Membr. Sci. 348 (2010) 298–309, https://doi.org/10.1016/j.memsci.2009.11.013.
[10] M.F. Gruber, C.J. Johnson, C.Y. Tang, M.H. Jensen, L. Yde, C. Hélix-Nielsen, Computational fluid dynamics simulations of flow and concentration polarization in forward osmosis membrane systems, J. Membr. Sci. 379 (2011) 488–495, https://doi.org/10.1016/j.memsci.2011.06.022.
[11] Y. Na, S. Yang, S. Lee, Evaluation of citrate-coated magnetic nanoparticles as draw solute for forward osmosis, Desalination 347 (2014) 34–42, https://doi.org/10.1016/j.desal.2014.04.032.
[12] S. Daer, N. Akther, Q. Wei, H.K. Shon, S.W. Hasan, Influence of silica nanoparticles on the desalination performance of forward osmosis polybenzimidazole membranes, Desalination 491 (2020) 114441, https://doi.org/10.1016/j.desal.2020.114441.
[13] P. Oymaci, K. Nijmeijer, Z. Borneman, Development of polydopamine forward osmosis membranes with low reverse salt flux, Membranes (Basel). 10 (2020) 94, https://doi.org/10.3390/membranes10050094.
[14] W.A. Suwaileh, D.J. Johnson, S. Sarp, N. Hilal, Advances in forward osmosis membranes: altering the sub-layer structure via recent fabrication and chemical modification approaches, Desalination 436 (2018) 176–201, https://doi.org/10.1016/j.desal.2018.01.035.
[15] M.M. Ling, K.Y. Wang, T.S. Chung, Highly water-soluble magnetic nanoparticles as novel draw solutes in forward osmosis for water reuse, Ind. Eng. Chem. Res. 49 (2010) 5869–5876, https://doi.org/10.1021/ie100438x.
[16] M. Son, T. Kim, W. Yang, C.A. Gorski, B.E. Logan, Electro-forward osmosis, Environ. Sci. Technol. 53 (2019) 8352–8361, https://doi.org/10.1021/acs.est.9b01481.
[17] S. Rampriyan, B. Ray, CFD investigations on a plate-and-frame forward osmosis module: effects of novel system parameters, J. Membr. Sci. Res. 9 (2023) 1–17, https://doi.org/10.22079/jmsr.2023.1999351.1601.
[18] M. Kahrizi, J. Lin, G. Ji, L. Kong, C. Song, L.F. Dumée, S. Sahebi, S. Zhao, Relating forward water and reverse salt fluxes to membrane porosity and tortuosity in forward osmosis: CFD modelling, Sep. Purif. Technol. 241 (2020) 116727, https://doi.org/10.1016/j.seppur.2020.116727.
[19] Y.Y. Liang, D.F. Fletcher, Computational fluid dynamics simulation of forward osmosis (FO) membrane systems: methodology, state of art, challenges and opportunities, Desalination 549 (2023) 116359, https://doi.org/10.1016/j.desal.2022.116359.
[20] H.K. Shon, S. Phuntsho, T.C. Zhang, R.Y. Surampalli, Forward osmosis: fundamentals and applications, American Society of Civil Engineers, Reston, VA (2015), https://doi.org/10.1061/9780784414071.
[21] J. Ren, M.R. Chowdhury, L. Xia, C. Ma, G.M. Bollas, J.R. McCutcheon, A computational fluid dynamics model to predict performance of hollow fiber membrane modules in forward osmosis, J. Membr. Sci. 603 (2020) 117973, https://doi.org/10.1016/j.memsci.2020.117973.
[22] M. Razmkhah, F. Moosavi, M.T.H. Mosavian, A. Ahmadpour, Does electric or magnetic field affect reverse osmosis desalination? Desalination 432 (2018) 55–63, https://doi.org/10.1016/j.desal.2017.12.062.
[23] M.E. Suk, N.R. Aluru, Effect of induced electric field on single-file reverse osmosis, Phys. Chem. Chem. Phys. 11 (2009) 8614–8619, https://doi.org/10.1039/b903541a.
[24] S. Zou, Z. He, Electrolysis-assisted mitigation of reverse solute flux in a three-chamber forward osmosis system, Water Res. 115 (2017) 111–119, https://doi.org/10.1016/j.watres.2017.02.060.
[25] J.L. Anderson, D.M. Malone, Mechanism of osmotic flow in porous membranes, Biophys. J. 14 (1974) 957–982, https://doi.org/10.1016/S0006-3495(74)85962-X.
[26] V. Sasidhar, E. Ruckenstein, Anomalous effects during electrolyte osmosis across charged porous membranes, J. Colloid Interface Sci. 85 (1982) 332–362, https://doi.org/10.1016/0021-9797(82)90003-0.
[27] P.M. Biesheuvel, S. Porada, M. Elimelech, J.E. Dykstra, Tutorial review of reverse osmosis and electrodialysis, J. Membr. Sci. 647 (2022) 120221, https://doi.org/10.1016/j.memsci.2021.120221.
[28] D. Burgreen, F.R. Nakache, Electrokinetic flow in ultrafine capillary slits 1, J. Phys. Chem. 68 (1964) 1084–1091, https://doi.org/10.1021/j100787a019.

[29] A.G. Guzmán-Garcia, P.N. Pintauro, M.W. Verbrugge, R.F. Hill, Development of a space-charge transport model for ion-exchange membranes, AICHE J. 36 (1990) 1061–1074, https://doi.org/10.1002/aic.690360713.
[30] P.B. Peters, R. Van Roij, M.Z. Bazant, P.M. Biesheuvel, Analysis of electrolyte transport through charged nanopores, Phys. Rev. E 93 (2016) 053108, https://doi.org/10.1103/PhysRevE.93.053108.
[31] A. Hill, Osmosis, Q. Rev. Biophys. 12 (1979) 67–99, https://doi.org/10.1017/S0033583500002602.
[32] G.M. Geise, Why polyamide reverse-osmosis membranes work so well, Science (80-.). 371 (2021) 31–32, https://doi.org/10.1126/science.abe9741.
[33] L. Wang, J. He, M. Heiranian, H. Fan, L. Song, Y. Li, M. Elimelech, Water transport in reverse osmosis membranes is governed by pore flow, not a solution-diffusion mechanism, Sci. Adv. 9 (2023) 1–12, https://doi.org/10.1126/sciadv.adf8488.
[34] H. Fan, M. Heiranian, M. Elimelech, The solution-diffusion model for water transport in reverse osmosis: what went wrong? Desalination 580 (2024) 117575 https://doi.org/10.1016/j.desal.2024.117575.
[35] S.H. Kim, S.Y. Kwak, T. Suzuki, Positron annihilation spectroscopic evidence to demonstrate the flux-enhancement mechanism in morphology-controlled thin-film-composite (TFC) membrane, Environ. Sci. Technol. 39 (2005) 1764–1770, https://doi.org/10.1021/es049453k.
[36] T.E. Culp, B. Khara, K.P. Brickey, M. Geitner, T.J. Zimudzi, J.D. Wilbur, S.D. Jons, A. Roy, M. Paul, B. Ganapathysubramanian, A.L. Zydney, M. Kumar, E.D. Gomez, Nanoscale control of internal inhomogeneity enhances water transport in desalination membranes, Science (80-.). 371 (2021) 72–75, https://doi.org/10.1126/science.abb8518.
[37] Y. Fang, L. Bian, Q. Bi, Q. Li, X. Wang, Evaluation of the pore size distribution of a forward osmosis membrane in three different ways, J. Membr. Sci. 454 (2014) 390–397, https://doi.org/10.1016/j.memsci.2013.12.046.
[38] S.J. Park, W. Choi, S.E. Nam, S. Hong, J.S. Lee, J.H. Lee, Fabrication of polyamide thin film composite reverse osmosis membranes via support-free interfacial polymerization, J. Membr. Sci. 526 (2017) 52–59, https://doi.org/10.1016/j.memsci.2016.12.027.
[39] L. Huang, J.R. McCutcheon, Impact of support layer pore size on performance of thin film composite membranes for forward osmosis, J. Membr. Sci. 483 (2015) 25–33, https://doi.org/10.1016/j.memsci.2015.01.025.
[40] V. Freger, G.Z. Ramon, The solution-diffusion model: "Rumors of my death have been exaggerated,", J. Membr. Sci. Lett. 4 (2024) 100084 https://doi.org/10.1016/j.memlet.2024.100084.
[41] I. Battiato, D.M. Tartakovsky, A.M. Tartakovsky, T.D. Scheibe, Hybrid models of reactive transport in porous and fractured media, Adv. Water Resour. 34 (2011) 1140–1150, https://doi.org/10.1016/j.advwatres.2011.01.012.
[42] M.T. Balhoff, K.E. Thompson, M. Hjortsø, Coupling pore-scale networks to continuum-scale models of porous media, Comput. Geosci. 33 (2007) 393–410, https://doi.org/10.1016/j.cageo.2006.05.012.
[43] T. Sun, Y. Mehmani, M.T. Balhoff, Hybrid multiscale modeling through direct substitution of pore-scale models into near-well reservoir simulators, Energy Fuel 26 (2012) 5828–5836, https://doi.org/10.1021/ef301003b.
[44] R.J. Hunter, Zeta potential in colloid science: principles and applications, Elsevier (1981), https://doi.org/10.1016/c2013-0-07389-6.
[45] Y.L. Zhang, S. Feng, Y. Tan, T.X. Cao, W. Ji, R. Xie, X.J. Ju, W. Wang, D.W. Pan, Z. Liu, L.Y. Chu, Programmable cation migration in unipolar 2D ion channels via dynamic Debye length, Chem. Commun. 61 (2025) 6763–6766, https://doi.org/10.1039/d5cc00667h.
[46] S. Di Fraia, N. Massarotti, P. Nithiarasu, Modelling electro-osmotic flow in porous media: a review, Int. J. Numer. Methods Heat Fluid Flow. 28 (2018) 472–497, https://doi.org/10.1108/hff-11-2016-0437.
[47] C.L. Rice, R. Whitehead, Electrokinetic flow in a narrow cylindrical capillary, J. Phys. Chem. 69 (1965) 4017–4024, https://doi.org/10.1021/j100895a062.
[48] C.E. Wyman, M.D. Kostin, Anomalous osmosis: solutions to the Nernst-Planck and Navier-stokes equations, J. Chem. Phys. 59 (1973) 3411–3413, https://doi.org/10.1063/1.1680484.
[49] E. GRIM, K. SOLLNER, The contributions of normal and anomalous osmosis to the osmotic effects arising across charged membranes with solutions of electrolytes, J. Gen. Physiol. 40 (1957) 887–899, https://doi.org/10.1085/jgp.40.6.887.
[50] Y. Kobatake, H. Fujita, Osmotic flow in charged membranes - I, Anomalous osmosis, Kolloid-Zeitschrift Zeitschrift Für Polym. 196 (1964) 58–64, https://doi.org/10.1007/BF01500027.
[51] N.A. Patankar, H.H. Hu, Numerical simulation of electroosmotic flow, Anal. Chem. 70 (1998) 1870–1881, https://doi.org/10.1021/ac970846u.
[52] S. Arulanandam, D. Li, Liquid transport in rectangular microchannels by electroosmotic pumping, Colloids Surfaces A Physicochem. Eng. Asp. 161 (2000) 89–102, https://doi.org/10.1016/S0927-7757(99)00328-3.
[53] H.M. Park, J.S. Lee, T.W. Kim, Comparison of the Nernst-Planck model and the Poisson-Boltzmann model for electroosmotic flows in microchannels, J. Colloid Interface Sci. 315 (2007) 731–739, https://doi.org/10.1016/j.jcis.2007.07.007.
[54] M. Heiranian, H. Fan, L. Wang, X. Lu, M. Elimelech, Mechanisms and models for water transport in reverse osmosis membranes: history, critical assessment, and recent developments, Chem. Soc. Rev. 52 (2023) 8455–8480, https://doi.org/10.1039/d3cs00395g.
[55] G.D. Mehta, T.F. Morse, Flow through charged membranes, J. Chem. Phys. 63 (1975) 1878–1889, https://doi.org/10.1063/1.431575.
[56] L. Wang, T. Cao, J.E. Dykstra, S. Porada, P.M. Biesheuvel, M. Elimelech, Salt and water transport in reverse osmosis membranes: beyond the solution-diffusion model, Environ. Sci. Technol. 55 (2021) 16665–16675, https://doi.org/10.1021/acs.est.1c05649.
[57] A. Mauro, Osmotic flow in a rigid porous membrane, Science 80 (149) (1965) 867–869, https://doi.org/10.1126/science.149.3686.867.
[58] F. Mugele, B. Bera, A. Cavalli, I. Siretanu, A. Maestro, M. Duits, M. Cohen-Stuart, D. Van Den Ende, I. Stocker, I. Collins, Ion adsorption-induced wetting transition in oil-water-mineral systems, Sci. Rep. 5 (2015) 10519, https://doi.org/10.1038/srep10519.
[59] G. Hurwitz, G.R. Guillen, E.M.V. Hoek, Probing polyamide membrane surface charge, zeta potential, wettability, and hydrophilicity with contact angle measurements, J. Membr. Sci. 349 (2010) 349–357, https://doi.org/10.1016/j.memsci.2009.11.063.
[60] D. Ebeling, D. Van Den Ende, F. Mugele, Electrostatic interaction forces in aqueous salt solutions of variable concentration and valency, Nanotechnology 22 (2011) 305706, https://doi.org/10.1088/0957-4484/22/30/305706.
[61] C. Yang, D. Li, Analysis of electrokinetic effects on the liquid flow in rectangular microchannels, Colloids Surfaces A Physicochem. Eng. Asp. 143 (1998) 339–353, https://doi.org/10.1016/S0927-7757(98)00259-3.
[62] S. Déon, A. Escoda, P. Fievet, A transport model considering charge adsorption inside pores to describe salts rejection by nanofiltration membranes, Chem. Eng. Sci. 66 (2011) 2823–2832, https://doi.org/10.1016/j.ces.2011.03.043.
[63] P.C. Jordan, How pore mouth charge distributions alter the permeability of transmembrane ionic channels, Biophys. J. 51 (1987) 297–311, https://doi.org/10.1016/S0006-3495(87)83336-2.
[64] F. Yu, H. Shi, J. Shi, K. Teng, Z. Xu, X. Qian, High-performance forward osmosis membrane with ultra-fast water transport channel and ultra-thin polyamide layer, J. Membr. Sci. 616 (2020) 118611, https://doi.org/10.1016/j.memsci.2020.118611.
[65] J. Song, M. Yan, J. Ye, S. Zheng, L.Y. Ee, Z. Wang, J. Li, M. Huang, Research progress in external field intensification of forward osmosis process for water treatment: a critical review, Water Res. 222 (2022) 118943, https://doi.org/10.1016/j.watres.2022.118943.
[66] J.B. Hasted, D.M. Ritson, C.H. Collie, Dielectric properties of aqueous ionic solutions. Parts I and II, J. Chem. Phys. 16 (1948) 1–21, https://doi.org/10.1063/1.1746645.
[67] S.P. Prasad, B.N. Singh, B.D. Singh, Effect of flow on the dielectric constant of liquids, Nature 147 (1941) 712, https://doi.org/10.1038/147712a0.
[68] P. Dutta, A. Beskok, T.C. Warburton, Numerical simulation of mixed electroosmotic/pressure driven microflows, Numer. Heat Transf. Part A Appl. 41 (2002) 131–148, https://doi.org/10.1080/104077802317221366.
[69] X. Xuan, D. Li, Electroosmotic flow in microchannels with arbitrary geometry and arbitrary distribution of wall charge, J. Colloid Interface Sci. 289 (2005) 291–303, https://doi.org/10.1016/j.jcis.2005.03.069.
[70] Y. Guan, T. Yang, J. Wu, Mixing and transport enhancement in microchannels by electrokinetic flows with charged surface heterogeneity, Phys. Fluids 33 (2021), https://doi.org/10.1063/5.0047181.
[71] J.A. Rard, D.G. Miller, The mutual diffusion coefficients of NaCl-H2O and CaCl2-H2O at 25°C from Rayleigh interferometry, J. Solut. Chem. 8 (1979) 701–716, https://doi.org/10.1007/BF00648776.
[72] J.A. Rard, D.G. Miller, The mutual diffusion coefficients of Na2SO4-H2O and MgSO4-H2O at 25°C from Rayleigh interferometry, J. Solut. Chem. 8 (1979) 755–766, https://doi.org/10.1007/BF00648779.
[73] A. Gorobchenko, S. Mareev, V. Nikonenko, Mathematical modeling of the effect of pulsed electric field on the specific Permselectivity of ion-exchange membranes, Membranes (Basel). 11 (2021) 115, https://doi.org/10.3390/membranes11020115.
[74] A. Aminnia, M. Khatibi, S. Nezameddin Ashrafizadeh, Fouling minimization with nanofluidic membranes; how electric field may help, Sep. Purif. Technol. 325 (2023) 124698, https://doi.org/10.1016/j.seppur.2023.124698.
[75] D. Rauly, M. Vindret, E. Chamberod, J.M.F. Martins, P. Xavier, Distribution of AC electric field-induced transmembrane voltage in Escherichia coli Cell Wall layers, Bioelectromagnetics 41 (2020) 279–288, https://doi.org/10.1002/bem.22261.
[76] A. Sagiv, A. Zhu, P.D. Christofides, Y. Cohen, R. Semiat, Analysis of forward osmosis desalination via two-dimensional FEM model, J. Membr. Sci. 464 (2014) 161–172, https://doi.org/10.1016/j.memsci.2014.04.001.
[77] B. Leasure, D.J. Kuck, S. Gorlatch, M. Cole, G.R. Watson, A. Darte, D. Padua, U. Banerjee, O. Schenk, K. Gärtner, D. Padua, H. Jay Siegel, B. Dalton Young, R. H. Campbell, Ü. Çatalyürek, C. Aykanat, J. Ajanovic, S. Schmid, R. Wattenhofer, E. N.M. Elnozahy, E.W. Speight, J. Li, R. Rajamony, L. Zhang, B. Arimilli, D. Padua, M. Gerndt, M. Gerndt, D. Padua, J.B. Dennis, B. Smith, G. Almasi, A. Stamatakis, D. Sangiorgi, D. Sangiorgi, D. Padua, J.A. Gunnels, J. Dongarra, P. Luszczek, B. Mohr, R. Eigenmann, P. Feautrier, C. Lengauer, D. Padua, P. Bose, J.F. JaJa, A. Gupta, R. De Nicola, D. Padua, D. Padua, D. Padua, R.S. Armen, E.R. May, M. Taufer, A. Geist, PARDISO, in: Encycl. Parallel Comput., Springer US, Boston, MA, 2011, pp. 1458–1464, https://doi.org/10.1007/978-0-387-09766-4_90.
[78] PARDISO, PARDISO 8.2, 2024.
[79] J.R. Bunch, L. Kaufman, Some stable methods for calculating inertia and solving symmetric linear systems, Math. Comput. 31 (1977) 163–179, https://doi.org/10.2307/2005787.
[80] Y.Y. Liang, Role of spacers in osmotic membrane desalination: advances, challenges, practical and artificial intelligence-driven solutions, Process. Saf. Environ. Prot. 201 (2025) 107587, https://doi.org/10.1016/j.psep.2025.107587.
[81] O. Lanzi, U. Landau, Effect of pore structure on current and potential distributions in a porous electrode, J. Electrochem. Soc. 137 (1990) 585–593, https://doi.org/10.1149/1.2086511.
[82] V. García-Morales, J. Cervera, J.A. Manzanares, Pore entrance effects on the electrical potential distribution in charged porous membranes and ion channels,

J. Electroanal. Chem. 599 (2007) 203–208, https://doi.org/10.1016/j.jelechem.2005.12.025.
[83] Q. Xiong, A.E. Lim, Y. Lim, Y.C. Lam, H. Duan, Dynamic magnetic Nanomixers for improved microarray assays by eliminating diffusion limitation, Adv. Healthc. Mater. 8 (2019), https://doi.org/10.1002/adhm.201801022.
[84] S. Xia, L. Yao, Y. Zhao, N. Li, Y. Zheng, Preparation of graphene oxide modified polyamide thin film composite membranes with improved hydrophilicity for natural organic matter removal, Chem. Eng. J. 280 (2015) 720–727, https://doi.org/10.1016/j.cej.2015.06.063.